THE EFFECT OF ICE CRYSTAL SURFACE ROUGHNESS ON THE RETRIEVAL OF ICE CLOUD MICROPHYSICAL AND OPTICAL PROPERTIES

A Thesis

by

YU XIE

Submitted to the Office of Graduate Studies of
Texas A&M University
in partial fulfillment of the requirements for the degree of

MASTER OF SCIENCE

May 2007

Major Subject: Atmospheric Sciences

THE EFFECT OF ICE CRYSTAL SURFACE ROUGHNESS ON THE RETRIEVAL OF ICE CLOUD MICROPHYSICAL AND OPTICAL PROPERTIES

A Thesis

by

YU XIE

Submitted to the Office of Graduate Studies of
Texas A&M University
in partial fulfillment of the requirements for the degree of

MASTER OF SCIENCE

Approved by:

Co-Chairs of Committee,	Ping Yang
	Gerald North
Committee Members,	Thomas Wilheit
	George Kattawar
Head of Department,	Richard Orville

May 2007

Major Subject: Atmospheric Sciences

ABSTRACT

The Effect of Ice Crystal Surface Roughness on the Retrieval of Ice Cloud Microphysical and Optical Properties. (May 2007)

Yu Xie, B.S., Peking University

Chair of Advisory Committee: Dr. Ping Yang

The effect of the surface roughness of ice crystals is not routinely accounted for in current cloud retrieval algorithms that are based on pre-computed lookup libraries. In this study, we investigate the effect of ice crystal surface roughness on the retrieval of ice cloud effective particle size, optical thickness and cloud-top temperature. Three particle surface conditions, smooth, moderately rough and deeply rough, are considered in the visible and near-infrared channels (0.65 and 3.75 μm). The discrete ordinates radiative transfer (DISORT) model is used to compute the radiances for a set of optical thicknesses, particle effective sizes, viewing and illumination angles, and cloud temperatures. A parameterization of cloud bi-directional reflectances and effective emittances is then developed from a variety of particle surface conditions. This parameterization is applied in a 3-channel retrieval method for Moderate Resolution Imaging Spectroradiometer (MODIS) data at 0.65, 3.75, and 10.8 μm. Cloud optical properties are derived iteratively for each pixel that contains ice clouds. The impact of ice crystal surface roughness on the cloud parameter retrievals is examined by comparing the results for particles with smooth surfaces and rough surfaces. Retrieval results from two granules of MODIS data indicate that the retrieved cloud optical thickness is significantly reduced if the parameterization for roughened particles is used, as compared with the case of smooth particles. For the retrieval of cloud effective particle size, the inclusion of the effect of surface roughness tends to decrease the retrieved effective particle size if ice crystals are small. The reversed result is noticed for large ice crystals. It is also found that surface roughness has a very minor effect on the retrieval of cloud-top temperatures.

ACKNOWLEDGMENTS

I thank my advisors, Dr. Ping Yang and Dr. Gerald North, for supporting this research and encouraging me to continue my education in Texas A&M University.

TABLE OF CONTENTS

Page

ABSTRACT………………………………………………………….................. iii

ACKNOWLEDGMENTS……………………………………………………….. v

TABLE OF CONTENTS………………………………………………………… vi

LIST OF FIGURES………………………………………………………………. vii

LIST OF TABLES……………………………………………………….......... xi

1. INTRODUCTION……………………………………………………………… 1

2. METHODOLOGY…………………………………………………………….. 5

2.1 Composite method…………………………………………………………... 5
2.2 Ice cloud reflectance and emittance…………………………………..……... 7
2.3 Radiative transfer solutions with phase function truncation…………..…….. 9
2.4 MODIS instrument and data……………………………………………..…. 16
2.5 Ice cloud property retrieval……………………………………………..…….. 17

3. PARAMETERIZATIONS OF REFLECTANCE AND EFFECTIVE EMITTANCE FOR ICE CLOUD……...………………………………………….. 25

3.1 Cloud microphysics and optical properties…………………………..…..…. 25
3.2 Ice cloud bidirectional reflectance…………………………………..…... 31
3.3 Ice cloud effective emittance………………………………………………. 33

4. EFFECT OF ICE CRYSTAL SURFACE ROUGHNESS ON MODIS RETRIEVAL………………………………………………………. 44

4.1 Effect of ice crystal surface roughness on the retrieval of ice cloud microphysical and optical properties…………………………………….. 44
4.2 Distributions of the retrieval results……………………………...………. 69

5. CONCLUSIONS AND DISCUSSION…………………………………………….. 78

REFERENCES………………………………………………………………………... 81

VITA……………………………………………………………………………….. 87

LIST OF FIGURES

FIGURE Page

1 Extinction and absorption efficiencies of hexagonal columns from the composite method based on the FDTD, Mie and IGOM (λ=6.7 μm)…………… 8

2 Comparison of bidirectional reflectances from DISORT with true coefficients, δ-fit truncation and δ-M truncation. Comparison of bidirectional reflectances from DISROT, Mishchenko's code and Adding doubling code……………………………………………………15

3 An example of cloud reflectance lookup table at 0.65 and 2.13 μm for various values of the cloud optical thickness and particle effective size………………………………………………………………………...19

4 Flow-chart of ice cloud property retrieval algorithm based on MODIS data channel 1, 20, 31……………………………………………………..22

5 Ice crystal bulk-scattering phase functions at λ=0.65 μm and λ=3.75 μm, De=21.9 μm……………………………………………………………………..29

6 Ice crystal bulk-scattering phase functions at λ=0.65 μm and λ=3.75 μm, De=155.9 μm……………………………………………………30

7 Bidirectional reflectances from parameterizations for surface smooth and moderately rough particles at $\mu_o = 0.65$, $\mu = 1.0$, $\varphi - \varphi_o = 0°$…………..……...32

8 Cloud bidirectional reflectances for (a) smooth, (b) moderately rough and (c) deeply rough particles at λ=0.65 μm, De=28.4 μm, μ_0=0.65, and τ=1.0……………………………………………………………………...34

9 Differences in cloud bidirectional reflectance between (a) moderately rough and smooth and (b) deeply rough and smooth particles at λ=0.65 μm, De=28.4 μm, μ_0=0.65, and τ=1.0………………………………………………..35

10 Cloud bidirectional reflectances for (a) smooth, (b) moderately rough and (c) deeply rough particles at λ=3.75 μm, De=28.4 μm, μ_0=0.65, and τ=1.0……………………………………………………………………36

11 Differences in cloud bidirectional reflectance between (a) moderately rough and smooth and (b) deeply rough and smooth particles at λ=3.75 μm, De=28.4 μm, μ_0=0.65, and τ=1.0………………………………………………..37

FIGURE Page

12 Effective emittances for all calculations at λ=3.75 μm and De = 46.33 μm……………………………………………………………..39

13 Effective emittances for all calculations at λ=10.8 μm and De = 46.33 μm……………………………………………………………..40

14 Variation of effective emittance with clear-cloud temperature difference for λ = 3.75 μm and De = 46.33 μm……………………………………………41

15 Variation of effective emittance with clear-cloud temperature difference for λ = 10.8 μm and De = 46.33 μm……………………………………………42

16 Brightness temperature differences from parameterizations for Ts = 300 K, Tc = 255 K, μ = 0.85………………………………………………………43

17 Clouds over the South Atlantic Ocean observed with MODIS Level 1b data on January 8, 2006…………………………………………………………45

18 MODIS cloud phase image for the granule shown in Figure 17………………..46

19 Ice cloud effective particle sizes obtained by using (a) surface smooth, (b) moderately rough, and (c) deeply rough particle models…………………....47

20 Differences between ice cloud effective particle sizes using (a) surface smooth and moderately rough, and (b) surface smooth and deeply rough particle models…………………………………………………………………...48

21 Relative differences between ice cloud effective particle sizes using (a) surface smooth and moderately rough, and (b) surface smooth and deeply rough particle models…………………………………………………49

22 Ice cloud optical thicknesses obtained by using (a) surface smooth, (b) moderately rough, and (c) deeply rough particle models…………………….50

23 Differences between ice cloud optical thicknesses using (a) surface smooth and moderately rough, and (b) surface smooth and deeply rough particle models………………………………………………………………………51

24 Relative differences between ice cloud optical thicknesses using (a) surface smooth and moderately rough, and (b) surface smooth and deeply rough particle models…………………………………………………52

25 Cloud-top temperatures obtained by using (a) surface smooth, (b) moderately rough, and (c) deeply rough particle models…………………….53

FIGURE Page

26 Differences between cloud-top temperatures using (a) surface smooth and moderately rough, and (b) surface smooth and deeply rough particle models……………………………………………………………………54

27 Relative differences between cloud-top temperatures using (a) surface smooth and moderately rough, and (b) surface smooth and deeply rough particle models…………………………………………………………………...55

28 Ice cloud over the South Indian Ocean observed with MODIS Level 1b data on January 11, 2005…………………………………………………………...58

29 MODIS cloud phase image for the granule shown in Fig. 28…………………...59

30 Ice cloud effective particle sizes obtained by using (a) surface smooth, (b) moderately rough, and (c) deeply rough particle models……………………60

31 Differences between ice cloud effective particle sizes using (a) surface smooth and moderately rough, and (b) surface smooth and deeply rough particle models…………………………………………………………………...61

32 Relative differences between ice cloud effective particle sizes using (a) surface smooth and moderately rough, and (b) surface smooth and deeply rough particle models……………………………………………………62

33 Ice cloud optical thicknesses obtained by using (a) surface smooth, (b) moderately rough, and (c) deeply rough particle models……………………63

34 Differences between ice cloud optical thicknesses using (a) surface smooth and moderately rough, and (b) surface smooth and deeply rough particle models…………………………………………………………………...64

35 Relative differences between ice cloud optical thicknesses using (a) surface smooth and moderately rough, and (b) surface smooth and deeply rough particle models………………………………………………..65

36 Cloud-top temperatures obtained by using (a) surface smooth, (b) moderately rough, and (c) deeply rough particle models……………………66

37 Differences between cloud-top temperatures using (a) surface smooth and moderately rough, and (b) surface smooth and deeply rough particle models……………………………………………………………………67

FIGURE Page

38 Relative differences between cloud-top temperatures using (a) surface smooth and moderately rough, and (b) surface smooth and deeply rough particle models…………………………………………………………...68

39 Histograms of (a) ice cloud effective particle sizes, (b) differences between ice cloud effective particle sizes using surface smooth and deeply rough particle models, (c) relative differences between ice cloud effective particle sizes using surface smooth and deeply rough particle models for the MODIS granule shown in Fig. 17………………..70

40 Histograms of (a) ice cloud optical thicknesses, (b) differences between ice cloud optical thicknesses using surface smooth and deeply rough particle models, (c) relative differences between ice cloud optical thicknesses using surface smooth and deeply rough particle models for the MODIS granule shown in Fig. 17………………………………..71

41 Histograms of (a) cloud-top temperatures, (b) differences between cloud-top temperatures using surface smooth and deeply rough particle models, (c) relative differences between cloud-top temperatures using surface smooth and deeply rough particle models for the MODIS granule shown in Fig. 17……………………………………………72

42 Histograms of (a) ice cloud effective particle sizes, (b) differences between ice cloud effective particle sizes using surface smooth and deeply rough particle models, (c) relative differences between ice cloud effective particle sizes using surface smooth and deeply rough particle models for the MODIS granule shown in Fig. 28……………………….75

43 Histograms of (a) ice cloud optical thicknesses, (b) differences between ice cloud optical thicknesses using surface smooth and deeply rough particle models, (c) relative differences between ice cloud optical thicknesses using surface smooth and deeply rough particle models for the MODIS granule shown in Fig. 28………………………………..76

44 Histograms of (a) cloud-top temperatures, (b) differences between cloud-top temperatures using surface smooth and deeply rough particle models, (c) relative differences between cloud-top temperatures using surface smooth and deeply rough particle models for the MODIS granule shown in Fig. 28………………………………………………..77

LIST OF TABLES

TABLE Page

1 Ice cloud models and effective sizes…………………………………………... 27

1. INTRODUCTION

Clouds have large global and temporal frequency of occurrence. They have been observed to cover about 30% of the Earth; in particular, clouds are observed in more than 50% of the satellite granules at mean and equatorial latitudes (Wylie et al. 1994, Liou, 1986). Clouds substantially reflect incident solar radiation at visible wavelengths. It was estimated that around 20% of the incoming solar radiation destined for the Earth's surface is directly reflected by clouds (Kiehl and Trenberth, 1997). At the same time, clouds also significantly absorb near-infrared and infrared radiation which inhibits the amount of energy emited from the Earth-atmosphere system. Due to their net radiative forcing, involving both the cooling and warming processes, clouds have a pronounced effect on the planetary radiative budget and therefore play a significant role in the terrestrial climate system and its evolution.

The study of determining the impact of clouds on climate is especially complicated because the microstructure of clouds is not well known. To understand the microphysics and its corresponding implications for Earth-atmosphere energy balance, remote sensing is widely used for monitoring cloud optical properties, which are quantified by cloud optical thickness, effective particle size, cloud-top temperature and ice water path in general circulation models.

Satellite-based cloud retrieval algorithms often require a function of cloud particle types in the forward radiative transfer models to simulate the bidirectional reflectances and effective emittances. The single-scattering albedo and phase function of water cloud

---

This thesis follows the style of *Journal of the Atmospheric Sciences*.

particles can be derived from Mie theory because of the simple spherical shape of water droplets. Realistic ice cloud particles, however, are almost exclusively nonsphercial particles with various complicated morphologies and polycrystals. Heymsfield and Platt (1984, Heymsfield, 1977) reported the representative data set for cirrus cloud particles observed by aircraft. The ice crystal samples, which were collected both in deep winter and spring time ice clouds, showed that hexagonal hollow columns and solid columns were predominantly found at temperatures below 223K. Some other particle habits, e.g., hexagonal plates and bullet rosettes were also collected at the top of the cloud. Thus, use of the single-scattering properties for non-spherical ice crystals becomes crucial in the study of ice clouds. Progress has been made toward the single-scattering computations involving a series of complex particle shapes. For example, Liou (1972) first assumed non-spherical ice crystals as long circular cylinders at visible and infrared wavelengths. He compared the phase functions of polydisperse spheres with the results associated with long circular cylinders and showed significant differences. Takano and Liou (1989) used a ray-tracing approach to develop an efficient scattering program for randomly and horizontally oriented hexagonal particles. Yang and Liou (1996) employed the finite-difference time domain (FDTD) method to the light scattering by bullet-rosettes, hexagonal plates, solid columns and hollow columns. Another issue for the study of ice clouds is bulk-scattering properties including the determination of ice crystal particle habit and size distribution, ice water content (IWC), effective particle size and single-scattering albedo. Minnis et al. (1998) developed a parameterization of reflectance and effective emittance for ice clouds on the basis of the integration of optical properties over

11 size distributions. The ice cloud particles are presented as hexagonal columns with a variety of aspect ratios according to in situ data.

Moreover, it is well known that cloud particles have rough surfaces because of the collision and coalescence processes. In most previous modeling efforts, however, ice crystals with smooth surfaces are commonly assumed. This approximation raises serious concerns about the effect of ice crystal surface roughness on the studies of ice particle single-scattering properties, radiative transfer and retrieval for various cloud microphysical properties. Perrin and Sivan (1991) derived the scattering properties of rough spheres obtained by randomly removing volume elements from the particle surface. The effect of surface roughness was shown by comparing the scattering properties of a rough surface sphere with those computed by Mie theory for a smooth surface sphere having the same particle size and refractive index. It was noted that the scattering intensities and polarizations of spheres are significantly affected by surface roughness and porosity in a certain spectral range around 0.22 μm. King et al. (2004) derived the MODIS collection 4 cloud products based on the ice cloud microphysical model with the effect of surface roughness accounted for. The particles used in the ice microphysical model were composed of 30% aggregates, 30% bullet rosettes, 20% hexagon hollow columns and 20% hexagonal plates, whereas in the calculation of the single-scattering properties for aggregates slight or moderate surface roughness conditions were included for each particle orientation. The ice crystal habits percentages and size distributions for individual habit used in the ice microphysical model were consistent with the in situ measurements from winter midlatitude and polar stratiorm ice clouds using a cloud particle imager (CPI) (Korolev and Isaac, 2003). Rolland et al.

(2000) estimated the uncertainty of the computed reflectance caused by surface roughness at the wavelengths of 0.65, 1.6 and 2.2 μm. In their study, the single-scattering properties of surface rough particles were computed by a perturbation technique developed by Liou et al. (1999). It was concluded that regardless of particle surface roughness causes a significant reduction of visible reflectances in most of the viewing angles used by satellite sensors.

The goal of this thesis is to improve the understanding of the effect of ice crystal surface roughness on the retrieval of cloud optical properties from MODIS data. We start by describing an approach to infer ice cloud optical properties along with some background information about the MODIS measurements. This presents a subset of the computing code used to carry out the research, including a composite method to calculate the single scattering properties, a phase function truncation method, and a radiative transfer solution for the simulation of cloud reflectance and emittance. An ice cloud microphysical retrieval model is then developed by using 0.65, 3.75 and 10.8 μm MODIS radiance measurements. Further, we demonstrate a parameterization of cloud reflectance and emittance in terms of cloud particle effective size, optical thickness, cloud-top temperature, surface temperature, ice crystal surface roughness and solar and satellite viewing angles. Finally, we compare the retrieval results for surface smooth, moderately rough and deeply rough particles. Comparisons of these results will improve our understanding of the effect of surface roughness on satellite-based cloud retrievals.

2. METHODOLOGY

The general methodology used to study the effect of ice crystal surface roughness on the retrieval of cloud microphysical and optical properties is to develop a 3-channel retrieval method based on the MODIS measurements at 0.65, 3.75, and 10.8 μm, and compare the retrieval by radiative transfer computations with different surface roughness conditions. In this section, we provide some background information on the composite method for the computation of single-scattering properties, the cloud bidirectional reflectance and effective emittance, and the MODIS data in visible, near-infrared and infrared channels. In addition, several radiative transfer models are compared with two single-scattering phase function truncation codes and therefore the most suitable model is used for this study. Furthermore, the ice cloud property retrieval algorithm first introduced by Minnis et al. (1995) is discussed.

2.1 Composite method

The single-scattering properties of hexagonal particles used in this study are computed by a composited method (Fu et al., 1998) with a combination of Mie theory (Wiscombe, 1979), an improved geometrical-optics method (IGOM) (Yang and Liou, 1996), and the finite difference time domain (FDTD) technique (Yang and Liou, 1996). The Mie code developed by Wiscombe (1979) computes the scattering of electromagnetic radiation from spheres. It has proved to be an efficient and accurate algorithm for homogeneous isotropic spheres in a large variety of wavelengths. For nonspherical particles, the FDTD technique (Yang and Liou, 1996), which solves the

Maxwell time-dependent curl equations by employing the finite-difference analog, has gained a reputation for being accurate but time-consuming. The IGOM (Yang and Liou, 1996) code along with a Geometric-optics-integral-equation hybrid method, however, because of computing efficiency requirement, is more applicable for nonspherical particles whose maximum dimensions are much larger than the incident wavelength.

A composited method for hexagonal particles is, therefore, suggested by Fu et al. (1998, Fu et al., 1999, Yang et al., 2005) for maximum efficiency and maintaining accuracy at the same time. The single-scattering properties for small particles with size parameter smaller than 30 are consistent with those calculated by the FDTD method. For large particles, Mie method, if employed to nonspherical particles, has proved to overestimate the tunneling effect (Guimaraes and Nussenzveig, 1992) while IGOM completely ignores this effect. Thus, the true value of the single-scattering property for a nonspherical particle is between that computed by the Mie method and IGOM with the same particle dimension. In this study, the composite method is assumed to be a linear combination of the results based on FDTD, Mie theory and IGOM. The extinction efficiency, absorption efficiency, and single-scattering albedo from the composite method are, respectively, given by

$$Q_e(L) = \begin{cases} Q_{eFDTD}(L) & (L < 30\lambda/\pi) \\ A_1 Q_{eMie}(L) + A_2 Q_{eIGOM}(L) & (L \geq 30\lambda/\pi) \end{cases}, \tag{1}$$

$$Q_a(L) = \begin{cases} Q_{aFDTD}(L) & (L < 30\lambda/\pi) \\ B_1 Q_{aMie}(L) + B_2 Q_{aIGOM}(L) & (L \geq 30\lambda/\pi) \end{cases}, \tag{2}$$

$$\varpi(L) = 1 - \frac{Q_a(L)}{Q_e(L)}, \tag{3}$$

where L is the maximum dimension of particle; $Q_{eFDTD}(L)$, $Q_{eMie}(L)$, and $Q_{eIGOM}(L)$ are extinction efficiencies computed by FDTD, Mie theory, and IGOM, respectively; $Q_{aFDTD}(L)$, $Q_{aMie}(L)$, and $Q_{aIGOM}(L)$ are absorption efficiencies computed by FDTD, Mie theory, and IGOM, respectively. The weighting coefficients A_1, A_2, B_1, and B_2, which are functions of incident wavelength, are determined in the overlapped region of FDTD and composite solutions. Fig. 1 shows the extinction and absorption efficiencies of hexagonal columns from the composite method at λ=6.7 μm. Following with Fu et al. (1998), the composite scheme takes the single-scattering phase functions and asymmetric factors from FDTD for size parameters smaller than 30 and those from IGOM for size parameters larger than 30.

2.2 Ice cloud reflectance and emittance

Bidirectional reflectance is defined as the ratio of the reflected intensity along a direction toward the detector to the incident intensity (Hapke, 1993), which implies a comparison of the reflected intensity from a surface with that from an absolutely white Lambertian surface. If the incident source of radiation is the sun, the bidirectional reflectance can be defined as follows:

$$R(\mu,\varphi;\mu_0,\varphi_0) = \frac{I(\mu,\varphi)}{\mu_0 F/\pi} = \frac{\pi I(\mu,\varphi)}{\mu_0 F}, \tag{4}$$

where $\mu = \cos\theta$ and $\mu_0 = \cos\theta_0$ in which θ_0 and θ are the solar and viewing zenith angles, respectively; φ_0 and φ are the azimuthal angles of the sun and the detector, respectively; F is the direct solar irradiance at the top of the atmosphere; and $I(\mu, \varphi)$ is the specific intensity emerging from the top of the atmosphere toward the detector. The reflectance factor is defined as normalized bidirectional reflectance, which is:

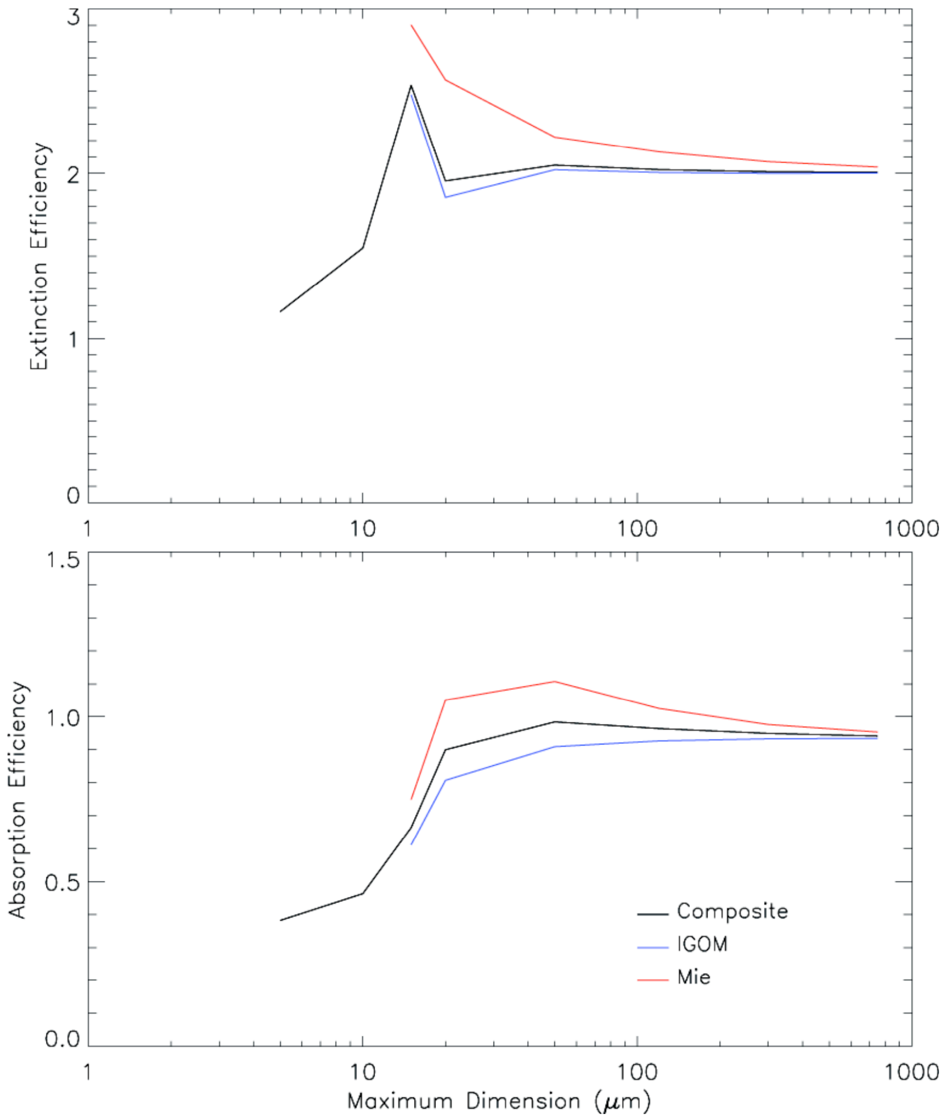

Fig. 1. Extinction and absorption efficiencies of hexagonal columns from the composite method based on the FDTD, Mie and IGOM (λ=6.7 μm).

$$\chi(\mu,\varphi;\mu_0,\varphi_0) = \frac{R(\mu,\varphi;\mu_0,\varphi_0)}{\alpha(\mu_0)}, \tag{5}$$

where $R(\mu, \varphi; \mu_0, \varphi_0)$ is bidirectional reflectance, $\alpha(\mu_o)$ is directional albedo computed by integrating bidirectional reflectance over the solar zenith angels.

For an infrared wavelength, the irradiance emitted from cloud and surface can be written

$$B(T) = \varepsilon B(T_{cld}) + (1-\varepsilon)B(T_{clear}), \tag{6}$$

where B(T) is the brightness observed at the top of the atmosphere (TOA), $B(T_{cld})$ is the Planck function associated with cloud temperature, $B(T_{clear})$ is the brightness at the TOA for clear sky condition, ε is emissivity or the ratio of the emitting intensity to the Planck function at the given wavelength. The cloud effective emittance determined by the emissivity in an emitting direction is then defined, at the same wavelength, as

$$\varepsilon(\mu) = \frac{B(T,\mu) - B(T_{clear},\mu)}{B(T_{cld},\mu) - B(T_{clear},\mu)}, \tag{7}$$

where μ is the cosine value of the viewing zenith angles.

Bidirectional reflectance and effective emittance of a medium are intrinsically associated with the reflectance, absorptance and roughness of the medium. Therefore, it provides valuable information on the optical characteristics of the medium. To compute the bidirectional reflectance and effective emittance associated with an ice cloud, this study assumes a plane-parallel layer composed of randomly oriented ice particles.

2.3 Radiative transfer solutions with phase function truncation

The intent of this section is first to validate the applicability of three existing radiative transfer codes, namely, DISORT (Stamnes et al., 1988), the adding-doubling model developed by de Hann et al. (1987), and an efficient computational model for a semi-infinite medium developed by Mishchenko et al. (2005). Because the bulk scattering phase function of ice crystals normally has a forward peak that is associated with the diffraction of the incident light for large size parameters, two truncation techniques, namely, the δ-M method developed by Wiscombe (1977) and the δ-fit method developed by Hu et al. (2000), are used to truncate the forward peak in this study. Therefore, it is important to find a combination of the Radiative Transfer Equation (RTE) solution and a phase function truncation method that is most appropriate for the numerical calculation of ice cloud microphysical and optical properties retrieval in this study.

2.3.1 DISORT

The DISORT model developed by Stamnes et al. (1988) is based on the discrete ordinates method pioneered by Chandrasekhar (1960). In this method, the specific intensity I is solved on the basis of the classical radiative transfer equation for a plane-parallel atmosphere, given by

$$\mu \frac{dI(\tau,\mu,\phi)}{d\tau} = I(\tau,\mu,\phi) - \frac{\tilde{\omega}}{4\pi}\int_0^{2\pi} d\phi' \int_{-1}^{1} I(\tau,\mu',\phi')P(\mu,\varphi;\mu',\phi')d\mu'$$

$$-\frac{\tilde{\omega}}{4\pi} FP(\mu,\phi;\mu',\phi')e^{-\tau/\mu_0} + (1-\tilde{\omega})B[T(\tau)], \tag{8}$$

where τ is the optical depth, $\tilde{\omega}$ is the single scattering albedo, F is the direct solar irradiance, and P is the phase function. Any application of the classical radiative transfer equation is based on an implicit assumption that scattering particles are located in each other's far-field zones (Mishchenko, 2002). However, particulate surfaces in nature are often composed of closely packed particles (Mishchenko, 1994, Garg et al., 1998). Preliminary analyses of the extent to which the classical radiative transfer equation can be applied to such closely packed scattering media have been reported in the literature, e.g., Li and Zhou (2004) and Zhang and Voss (2005).

In the framework of the DISORT model, the specific intensity is expanded in a Fourier series as follows:

$$I(\tau;\mu,\phi) = \sum_{m=0}^{N} I^m(\tau,\mu)\cos m(\phi_0 - \phi). \tag{9}$$

By expanding the phase function in Eq. (8) and replacing the integral by Gaussian quadrature, each I^m coefficient can be solved independently in the form of the summation of all the homogeneous solutions and the particular solutions for the multiple-scattered radiation associated with the incident radiation and thermal emission as follows:

$$I^m(\tau,\mu_i) = \sum_j L_j^m \varphi_j^m(\mu_i) e^{-k_j^m \tau} + Z^m(\mu_i) e^{-\tau/\mu_0} \text{ , i = -n,…,n.} \tag{10}$$

The DISORT is applicable to an atmosphere with various layers of arbitrary values of optical thickness, single-scattering albedo, and phase function. Extensive efforts have been carried out to validate the applicability and accuracy of this radiative transfer computational model. The technical details of the DISORT are not recapitulated here since they have been reported in the literature (Stamnes et al., 1988).

2.3.2 DISORT with δ-fit truncation

The scattering phase function in DISORT is specified in terms of its Legendre polynomial expansion coefficients. For a phase function with a strong forward peak, thousands of Legendre expansion terms are required. To use a practical number of expansion terms, which means less computer CPU time, the truncation of the forward peak is required. The DISORT computational package contains the δ-M truncation scheme (Wiscombe, 1977). This study uses the δ-fit truncation scheme (Hu et al., 2000) that is an extension and enhancement of the δ-M scheme. However, different from the δ-M truncation, the δ-fit technique provides the coefficients of Legendre expansion by solving the following equations:

$$\frac{\partial \varepsilon}{\partial c_l} = 0, \quad l=0,\ 1,\ 2,\ldots,\ N \tag{11}$$

where ε is the relative difference between actual phase function and truncated phase function. C_l, $l=0, 1, 2, \ldots, N$ are the coefficients of the Legendre polynomial expansion of the truncated phase function. It is evident from Eq. (11) that the δ-fit technique minimizes the errors associated with the truncation.

2.3.3 Adding-doubling method

The adding-doubling method for solving the RTE was introduced by van de Hulst (1963). The adding-doubling computational program used in this study was developed by de Haan et al. (1987) and fully accounts for polarization which is a sine qua non for the transfer of radiation. In practice, the doubling method may start with a thin layer of known single-scattering albedo and phase matrix, although Kattawar and Plass (1973) showed that this initialization scheme has some disadvantages and suggested a more appropriate approach. Consider combining two parallel layers, one placed on top of the other. Let R_1 and T_1 be the reflection and transmission functions, respectively, for the first layer; whereas R_2 and T_2 are those for the second layer. The bidirectional reflectance and transmission functions of the combined layer are given by employing the adding equations (Eq. (19)-(25) in de Haan et al. (1987)) using R_1, T_1, R_2 and T_2. The reflection and transmission function of a layer with known single-scattering properties but arbitrary optical thickness can be calculated by adding thin layers until the desired optical thickness is reached. The doubling method is a special case of the adding method when the conjoined layers may have the same optical properties, i.e., optical thickness, single-scattering albedo, and phase function.

To reduce the number of integrations in the adding scheme, a Fourier expansion is used in the computational code developed by de Haan et al. (1987). For each Fourier component, a set of azimuth-independent adding equations is derived. The supermatrices are employed to treat the combinations of integrations and matrix multiplications as single matrix products.

Similar to DISORT, the adding-doubling method is also a rigorous method for radiation transfer calculations. One of the advantages of this method is that it is quite effective for computing the reflection or transmission function of a system composed of various vertically inhomogeneous layers.

2.3.4 Mishchenko et al.'s method

A radiative transfer computational package developed by Mishchenko et al. (1999) is quite efficient for computing the bidirectional reflectance of a semi-infinite homogeneous particulate medium. This technique is based on the fact that the bidirectional reflectance can be expanded in a Fourier series as follows:

$$R(\mu,\mu_0,\phi) = R^0(\mu,\mu_0) + 2\sum_{m=1}^{m_{\max}} R^m(\mu,\mu_0)\cos m\phi . \tag{12}$$

The coefficients R^m in Eq. (12) can be determined directly by solving Ambarzumian's nonlinear integral equation (Yanovitskij, 1997, Mishchenko, 2005).

Unlike the DISORT and adding-doubling computational programs, the computational technique developed by Mishchenko et al. (1999) is restricted to homogeneous semi-infinite scattering layers. However, the advantage of the latter is that the computation of the internal radiation field is avoided, and the efficiency in numerical computation is improved.

2.3.5 Comparison

Figure 2 shows the comparison of the performance of the aforementioned three RT computational models (Xie et al., 2006). Canonical simulations are carried out with an optical thickness of 2000, single-scattering albedo of 1, and the Henyey-Greenstein (H-G) phase function, with a g of 0.75. The H-G function can be given in the form

$$P(\cos\Theta) = \frac{1-g^2}{(1+g^2-2g\cos\Theta)^{3/2}} = \sum_{l=0}^{N}(2l+1)g^l P_l(\cos\Theta). \tag{13}$$

Evidently, the Legendre expansion coefficients of the H-G function can be obtained exactly, provided the asymmetry factor is given. For this analytical phase function, hundreds of Legendre expansion coefficients in DISORT are needed to give convergent results. Figure 2 shows the DISORT with an 8-term expansion of the phase function based on the δ-fit method which essentially converges to the correct solution with several hundred expansion terms. From the comparison of the results from DISORT with δ-fit (dotted line in Fig. 2) and δ-M (dashed line) truncation methods, it is evident that the δ-fit truncation scheme is more accurate when the same number of expansion terms are used. Thus, the δ-fit truncation scheme is used in both Mishchenko et al.'s method and the

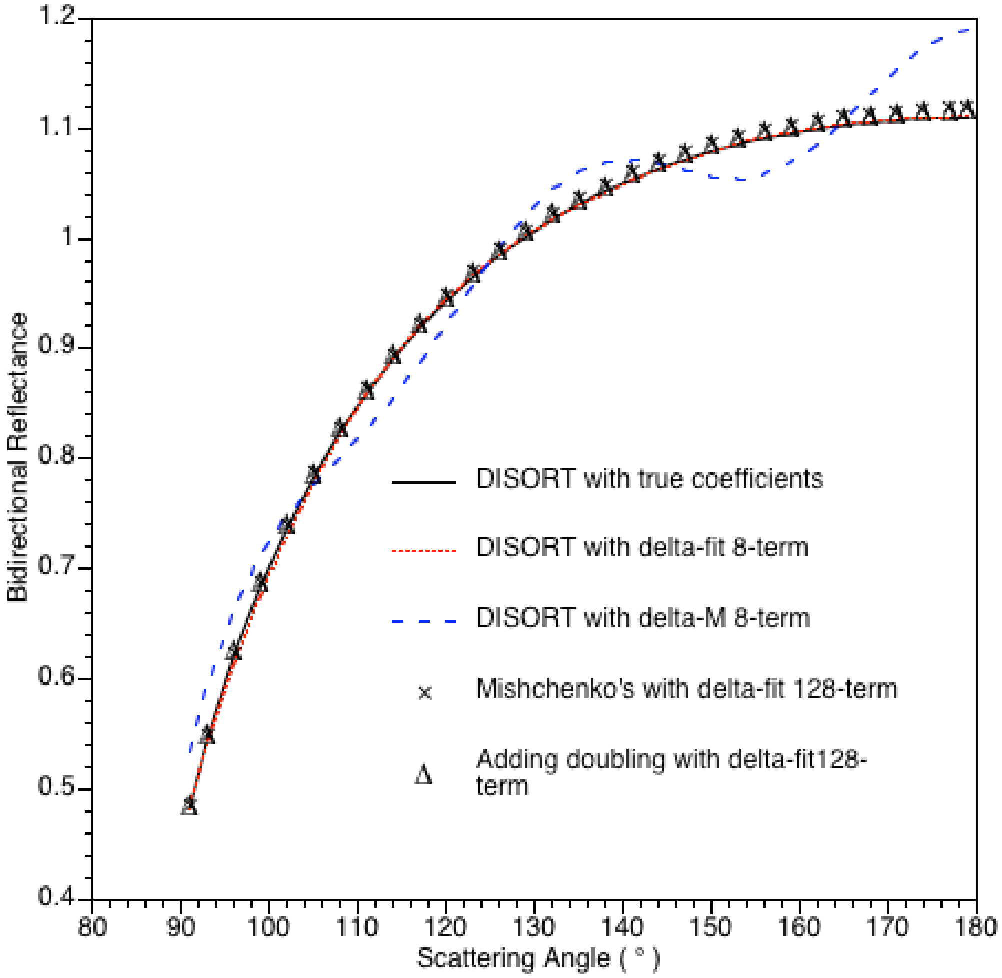

Fig. 2. Comparison of bidirectional reflectances from DISORT with true coefficients, δ-fit truncation and δ-M truncation. Comparison of bidirectional reflectances from DISROT, Mishchenko's code and Adding doubling code.

adding-doubling code in this study. To achieve high accuracy, 128 expansion terms are considered in the δ-fit truncation coefficients. Evidently, the aforementioned three radiative transfer models agree well with each other. However, Mishchenko et al.'s method is only suitable for a case with a semi-infinite optical thickness. Thus, for an ice cloud that is optically thin, a combination of the DISORT and the δ-fit expansion with 128 terms is utilized in this study.

2.4 MODIS instrument and data

The Moderate Resolution Imaging Spectrometer (MODIS), developed for the NASA-centered international Earth Observing System (EOS), is one of the instruments aboard the Terra and Aqua satellites. The Terra spacecraft, managed by NASA's Goddard Space Flight Center, was launched on December 18, 1999, with five instruments. It circles the Earth from north to south and crosses the equator in the morning when the view of the surface is least obstructed by cloud cover. Aqua, lauched on May 4, 2002, is the latest in the series of EOS spacecraft. Same as the Terra satellite, Aqua's orbit is roughly perpendicular to the direction of Earth's spin, but crosses the equator at 1:30 p.m. local time, which, combined with Terra, provides important insights into the daily cycling of the Earth's system. Terra and Aqua are collecting data in a 705-kilometer orbit and viewing the entire Earth's surface every 1 to 2 days.

The MODIS instrument is a scanning radiometer with a two-sided scan mirror, making a ±55° scanning pattern at the orbit of Terra and Aqua. MODIS has 36 bands ranging in wavelength from 0.414 μm to 14.235 μm (Ardanuy et al., 1991, King et al., 1992, King et al, 2003). The bands centered at 0.65 and 0.86 μm have a nadir spatial resolution of 250 m, while the bands centered at 0.47, 0.56, 1.24, 1.63, and 2.13 μm have a nadir spatial resolution of 500 m. The other 29 bands, including all the bands at infrared wavelengths, have 1000 m spatial resolution. According to the processing levels, MODIS data is provided as Level-0, Level-1, Level-2, and Level-3 data. MODIS data, observed from the Terra and Aqua spacecrafts, is first transmitted to ground station in White Sands, NM, and then processed into Level 0 data at the EOS DATA and Operations System (EDOS). Subsequently, the EDOS at the Goddard Space Flight Center produces the Level-1A data that contains the radiances and brightness temperatures for all 36 bands. The MODIS Calibration Support Team (MCST) then applies calibration to Level-1A data and provides the corresponding Level-1B data that has been geolocated in 5-min granules. Following the same resolution and location of the Level-1 data, MODIS Level-2 data consists of the geophysical products including cloud mask, aerosol product, total precipitable water, cloud product, and atmospheric profiles. Finally, MODIS Level-3 data is spatially averaged from Level-2 data at daily, weekly, monthly, annual, or seasonal time intervals. In this study, the ice cloud microphysical and optical properties is retrieved by using the bidirectional reflectances and brightness temperature from MODIS Level-1B data and cloud mask from Level-2 data for distinguishing clouds from a clear sky.

2.5 Ice cloud property retrieval

Some previous studies have demonstrated the determination of cloud microphysical and optical properties from satellite solar or infrared radiation measurements. For example, Nakajiam and King (1990) derived cloud optical thickness and particle effective size of water clouds from satellite reflection measurements at visible and near-infrared channels. In their study, wavelengths of 0.75 and 2.16 μm are taken without considering the atmospheric profile because they are outside of the water vapor and oxygen absorption region. It is evident that the reflectance at 0.75 μm is sensitive to cloud optical thickness but little dependent on effective particle size. At the wavelength of 2.16 μm, however, the reflectance is sensitive to effective particle size while showing less sensitivity to cloud optical thickness because of the different refractive index and the absorption characteristics of that band. The cloud optical thickness and effective size can then be determined independently from the results of the reflectance at 0.75 and 2.16 μm, respectively. With this method, the measurement and computing error has little impact on the retrieval results because the cloud properties are all determined when they are sensitive to cloud reflectance. Thus, a lookup library of simulated solar reflectances is created in these two bands. By integrating and checking the values on the lookup table, it is possible to confidently retrieve the cloud optical thickness and effective particles size from the satellite measurements in the specific solar and viewing zenith angles and relative azimuth angles. Fig. 3 is an example of the simulated cloud reflectance lookup table for various values of cloud optical thickness and particle effective size.

The lookup table retrieval method based on the radiation simulation in two solar channels has been employed in numerous studies on remote sensing and extended to infrared wavelengths in order to make use of MODIS nighttime data (Wei et al., 2004, Huang et al., 2004, Meyer et al., 2004). However, cloud property retrieval involving only two solar or infrared channels may ignore the determination of cloud height and its

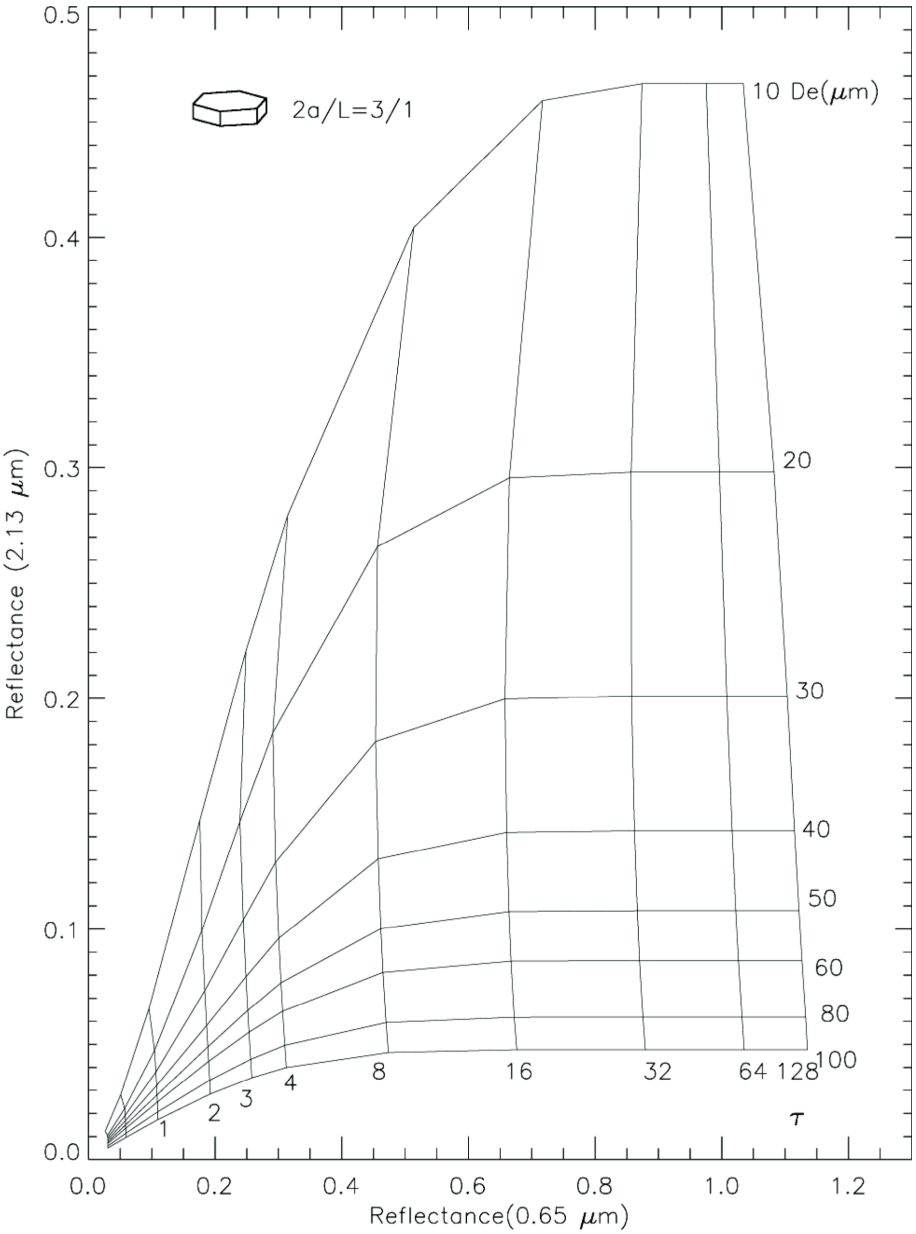

Fig. 3. An example of cloud reflectance lookup table at 0.65 and 2.13 μm for various values of the cloud optical thickness and particle effective size.

impact on the retrieval of cloud microphysical and optical properties. Therefore, in this study, a 3-channel retrieval method was developed based on parameterizations of ice cloud bidirectional reflectance and effective emittance, which can solve cloud height as well as cloud optical thickness and effective particle size from the MODIS measurements. This retrieval method, which was first introduced by Minnis et al. (1995, Minnis et al., 1998), uses visible, near-infrared and infrared wavelengths at 0.65, 3.75, and 10.8 μm, respectively.

For visible band, 0.65 μm, the spectral bidirectional reflectance has been described by Eqn. (4). As mentioned above, visible wavelength shows much sensitivity to optical thickness. Thus, the value of optical thickness at that wavelength can be determined by matching the bidirectional reflectance measurements from MODIS channel 1 to a parameterization of cloud bidirectional reflectance with certain effective particle size, cloud height and surface albedo. The details of ice cloud parameterization will be discussed in section 3, including the ice crystal single-scattering property, the determination of particle size and habit distributions, the values of cloud bidirectional reflectance and effective emittance respectively for solar and infrared wavelength, and the sensitivity of particle surface roughness to the parameterization. The effect of atmospheric gases is ignored because of little absorption in the visible channel. Following with Nakajiam and King (1990), the underlying surface, in this study, is restricted to an ocean surface with surface albedo of 0.06.

The simulated upwelling brightness at the top of the atmosphere (TOA) can be simplified in the infrared band at 10.8 μm by,

$$B_{31}(T)=\varepsilon_{31}(\mu, De, \tau)\ B_{31}(T_c) + (1- \varepsilon_{31}(\mu, De, \tau)\ )\ \varepsilon_0 B_{31}(T_{clear}), \qquad (14)$$

where T_c is the cloud temperature, $B_{31}(T_{clear})$ is the brightness for clear-sky condition at the TOA, ε_0 is the surface emittance, $\varepsilon_{31}(\mu, De, \tau)$ is cloud effective emittance which is a function of cloud optical thickness, effective particle size and viewing zenith angle. The clear-sky brightness $B_{31}(T_{clear})$ is computed by DISORT where the absorption caused by the atmosphere gases is calculated by correlated-k distribution developed by Kratz (1995). It is evident that the infrared radiance is sensitive to cloud temperature.

Both solar radiation and thermal emission have to be accounted for in the near-infrared band of 3.75 μm. With the effect of solar reflectance, Eqn (14) can be improved in the MODIS channel 20 by,

$$B_{20}(T) = \varepsilon_{20}(\mu, De, \tau)\, B_{20}(T_c) + (1- \varepsilon_{20}(\mu, De, \tau))\varepsilon_0 B_{20}(T_{clear}) + \mu_0 E_0\, R_{20}(\mu_0, \mu, \varphi, De, \tau)/\pi, \tag{15}$$

where $B_{20}(T)$ is the brightness observed at the TOA, T_c is the cloud temperature, $B_{20}(T_{clear})$ is the brightness for clear-sky condition at the TOA, $\varepsilon_{20}(\mu, De, \tau)$ is cloud effective emittance, E_0 is the solar spectral irradiance at 3.75 μm. $R_{20}(\mu_0, \mu, \varphi, De, \tau)$ is the bidirectional reflectance at the top of the cloud which is a function of cloud optical thickness, cloud effective particle size, solar and viewing zenith angle, and relative azimuth angle. Again, correlated-k distribution is used to correct the radiative transfer computation for atmospheric absorption in the near-infrared channel. The advantage of taking the 3.75 μm channel is that the cloud emittance in this channel is more sensitive to cloud optical thickness and effective particle size than at infrared wavelength.

In the 3-channel retrieval method, the cloud optical thickness, effective particle size and cloud top temperature are iteratively determined from the MODIS measurements of 0.65, 3.75, and 10.8 μm, respectively. Fig. 4 shows the Flow-chart of ice cloud

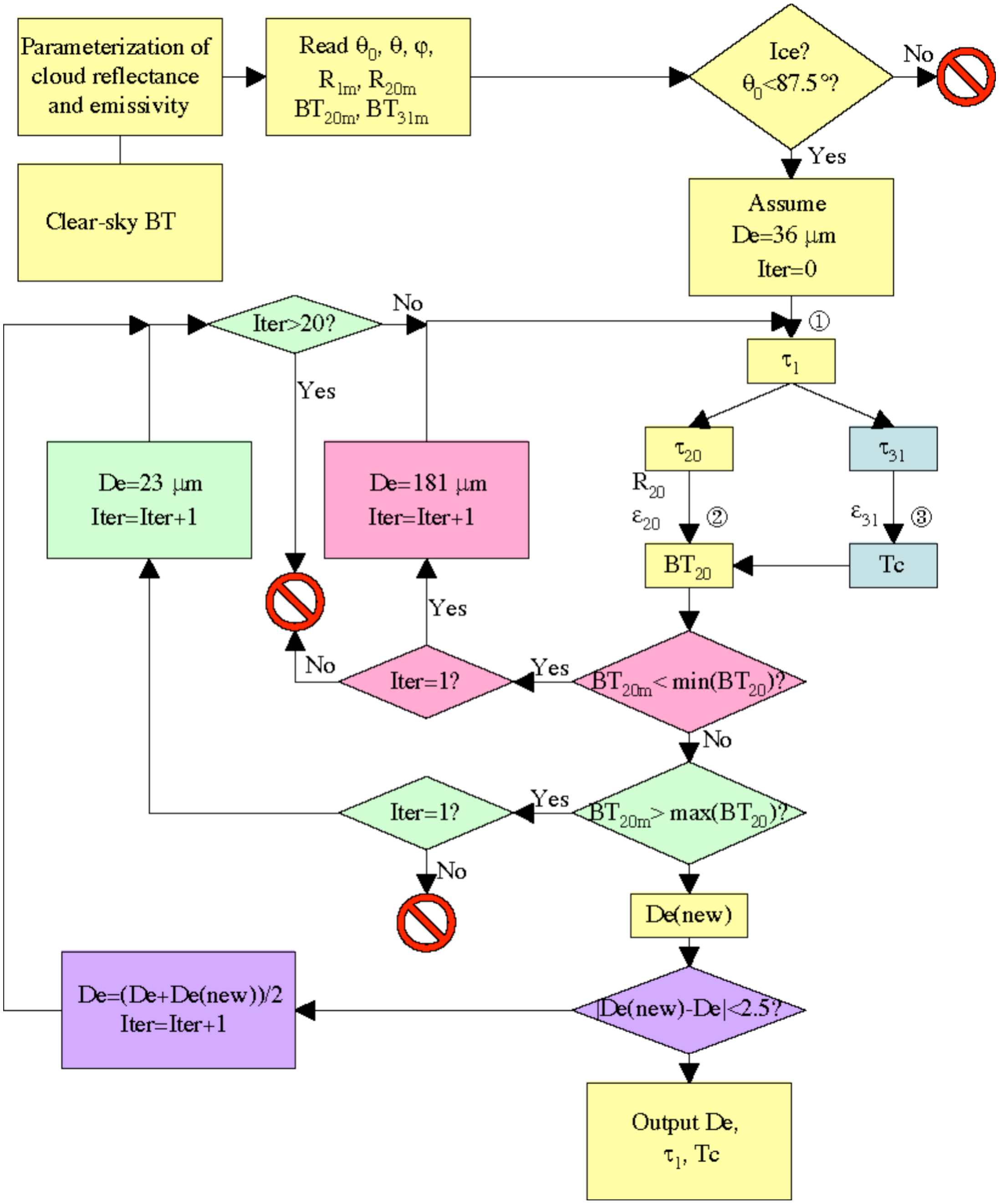

Fig. 4. Flow-chart of ice cloud property retrieval algorithm based on MODIS data channel 1, 20, 31. ① 0.65 μm (MODIS band 1): $R_1(\mu_0, \mu, \varphi, De, \tau)$. ② 3.75 μm (MODIS band 20): $B_{20}(T) = \varepsilon_{20}(\mu, De, \tau)\ B_{20}(T_c) + (1- \varepsilon_{20}(\mu, De, \tau))\varepsilon_0 B_{20}(T_{clear}) + \mu_0 E_0\ R_{20}(\mu_0, \mu, \varphi, De, \tau)/\pi$. ③ 10.8 μm (MODIS band 31): $B_{31}(T)=\varepsilon_{31}(\mu, De, \tau)\ B_{31}(T_c) + (1- \varepsilon_{31}(\mu, De, \tau))\varepsilon_0 B_{31}(T_{clear})$.

property retrieval algorithm based on MODIS data channel 1 (0.65 μm), 20 (3.75 μm), 31(10.8 μm). The first step of the 3-channel retrieval method is to parameterize ice cloud bidirectional reflectance and effective emittance for solar and infrared wavelengths, respectively. The parameterization is then interpolated at cloud optical thickness, effective particles size, cloud top temperature, surface temperature, and solar and satellite viewing angles. The retrieval process starts with an initial guess of effective particle size De = 37 μm, if the MODIS Level-2 data shows that it is covered by an ice cloud in the pixel and the solar zenith angle is less than 87.5°. A cloud optical thickness of 0.65 μm can be retrieved for that pixel by reading the satellite observed measurement and matching it to the simulated bidirectional reflectance for the solar and viewing angles. The optical thickness for an infrared wavelength is therefore derived from the visible optical thickness by

$$\tau = \frac{\tau_{vis} Q}{Q_{vis}}, \tag{16}$$

where Q and Q_{vis} is the extinction efficiency for infrared and visible wavelengths, respectively. With an assumed effective particle size and the optical thickness in that channel, the cloud top temperature can be solved from Eqn (14). The 3.75 μm radiance at the TOA is then recomputed by using Eqn (15) with the retrieved cloud optical thickness and cloud top temperature. That radiance can give a new effective size by comparison with the MODIS measurement at 3.75 μm. If the value of the new effective size is very close to the assumed one, then the retrieved properties, including cloud optical thickness, effective particle size and cloud top temperature, will be effected. Otherwise, the retrieval model will adjust the effective particle size and repeat the process until the assumed value of effective particle size matches the derived one.

One of the advantages of this 3-channel retrieval method is that it consumes much less time than simply matching the radiances at a two-wavelength lookup table, e.g. Fig. 3. This retrieval method iteratively checks the simulations from one-column tables, which is much faster than checking in a two-dimensional matrix. The computing time of the retrieval mostly depends on how many interpolations have been done in the parameterizations of the cloud bidirectional reflectance and effective emittance. For example, cloud bidirectional reflectance in this study is a function of cloud optical thickness, cloud effective particle size, solar and satellite viewing zenith angle, and relative azimuth angle. If the interpolations for all five quantities have been precomputed and saved on a hard drive, the checking and matching processes will be very fast. And the retrieval of cloud properties for a whole granule of MODIS data may just take a few minutes. However, because of the limitation of hard drive space, only three of the five quantities have been done while the other two have to be computed before doing the retrieval. Therefore, the computing of the retrieval for a granule of MODIS data may take a couple of hours in this study.

3. PARAMETERIZATIONS OF REFLECTANCE AND EFFECTIVE EMITTANCE FOR ICE CLOUD

The intention of this section is to parameterize the cloud bidirectional reflectance and effective emittance for ice clouds with various particle surface roughness conditions. This parameterization is going to be used in the retrieval of ice cloud optical thickness, effective particle size and cloud-top temperature in Section 4.

3.1 Cloud microphysics and optical properties

The ice cloud particle shapes considered in the present computation are hexagonal columns with the aspect ratios, L/2a, of 5 μm / 5 μm, 10 μm / 5 μm, 10 μm / 10 μm, 20 μm / 20 μm, 50 μm / 40 μm, 120 μm / 60 μm, 300 μm / 100 μm, and 750 μm / 160 μm. The single-scattering properties of ice particles are computed from IGOM in the visible channel (0.65 μm), and a composite method that is based on the FDTD technique, IGOM, and Lorenz-Mie theory in the near-infrared through far-infrared wavelength regime (3.75 μm, and 10.8 μm). Three particle surface conditions, smooth, moderate rough and deeply rough, are considered in the visible and near-infrared channels (0.65 μm and 3.75 μm). The single-scattering properties are then integrated over a variety of ice crystal size distributions, which have been extensively studied by Minnis et al. (1998). The bulk optical properties for a given particle size distribution n(L) are determined as follows:

$$De = \frac{3\int_{L_{\min}}^{L_{\max}} V(L)n(L)dL}{2\int_{L_{\min}}^{L_{\max}} A(L)n(L)dL}, \tag{17}$$

$$\langle Q_e \rangle = \frac{\int_{L_{\min}}^{L_{\max}} Q_e(L)A(L)n(L)dL}{\int_{L_{\min}}^{L_{\max}} A(L)n(L)dL}, \tag{18}$$

$$\langle Q_a \rangle = \frac{\int_{L_{\min}}^{L_{\max}} Q_a(L)A(L)n(L)dL}{\int_{L_{\min}}^{L_{\max}} A(L)n(L)dL}, \tag{19}$$

$$\langle g \rangle = \frac{\int_{L_{\min}}^{L_{\max}} g(L)Q_s(L)A(L)n(L)dL}{\int_{L_{\min}}^{L_{\max}} Q_s(L)A(L)n(L)dL}, \tag{20}$$

$$\langle \omega \rangle = \frac{\int_{L_{\min}}^{L_{\max}} Q_s(L)A(L)n(L)dL}{\int_{L_{\min}}^{L_{\max}} Q_e(L)A(L)n(L)dL}, \tag{21}$$

$$\langle f \rangle = \frac{\int_{L_{\min}}^{L_{\max}} f(L)Q_s(L)A(L)n(L)dL}{\int_{L_{\min}}^{L_{\max}} Q_s(L)A(L)n(L)dL}, \tag{22}$$

where *De* is particle effective size, *V* is particle volume, *A* is projected area, *Qe* is extinction efficiency, *Qa* is absorption efficiency, *g* is the asymmetry factor, ω is single-scattering albedo, and factor *f* is associated with delta-transmission of the incident rays through two parallel faces of the scattering particle. The definition of effective particles size in Minnis et al. (1998) is

$$De = \frac{\int_{L_{\min}}^{L_{\max}} D \times LDn(L)dL}{\int_{L_{\min}}^{L_{\max}} D \times Ln(L)dL}, \tag{23}$$

where D is the width of the particle. The ice cloud particle effective sizes from Minnis et al. (1998) and computations in this study are given in Table 1. Eleven ice crystal size distributions based on in situ measurements are given. The details of those 11 size distributions are not discussed because they have been extensively studied in previous studies (Minnis et al., 1998, Takano and Liou, 1989, Heymsfield and Platt, 1984, Ou et

Table 1. Ice cloud models and effective sizes.

Model	De (μm) (Minnis et. al, 1998)	De (μm) (in this study)
NCON	5.83	5.64
CON	18.15	16.68
CC	23.86	21.86
T60	30.36	28.40
CS	41.20	40.35
WCS	45.30	46.34
T40	67.6	65.29
NOV	75.2	80.31
OCT	104.9	115.32
CU	123.1	140.15
LPC	134.9	155.95

al., 1993, Poelot and Henderson, 1994). The differences of the two sets of particle effective sizes in table 1 are caused only by the difference between Eq. (17) and (23).

Figure 5 compares the bulk-scattering phase functions of surface smooth particles with moderately rough and deeply rough surface particles. The effective particle size, De=21.9 μm, associated with particle size distribution of cold cirrus (CC) is taken at visible and near-infrared wavelengths of λ=0.65 μm and λ=3.75 μm, respectively. It is evident that the surface roughness condition largely affects the scattering properties of hexagonal ice crystals. For the smooth case, the pronounced 22° scattering peak and 46° halo peak is seen as a general feature of the phase function for ice crystals. For the moderately rough case, the 46° scattering peak is smoothed out in the phase function although a broad scattering maximum 22° is still noticeable. For the deeply rough case, the computed phase function is essentially featureless. Furthermore, the backscattering is substantially reduced for the rough surface cases which physically is because of the spreading of the collimatic light beams. It is also displayed in Fig. 5 that the phase function of ice crystals at near-infrared wavelength is much more sensitive than that at visible wavelength. Fig. 6 is the same as Fig. 5 except that the effective particle size is taken as De=155.9 μm, which is associated with particle size distribution of large particle cirrus (LPC). It is evident that the bulk-scattering phase functions of both large and small particles would be affected by taking surface roughness into the computation of scattering.

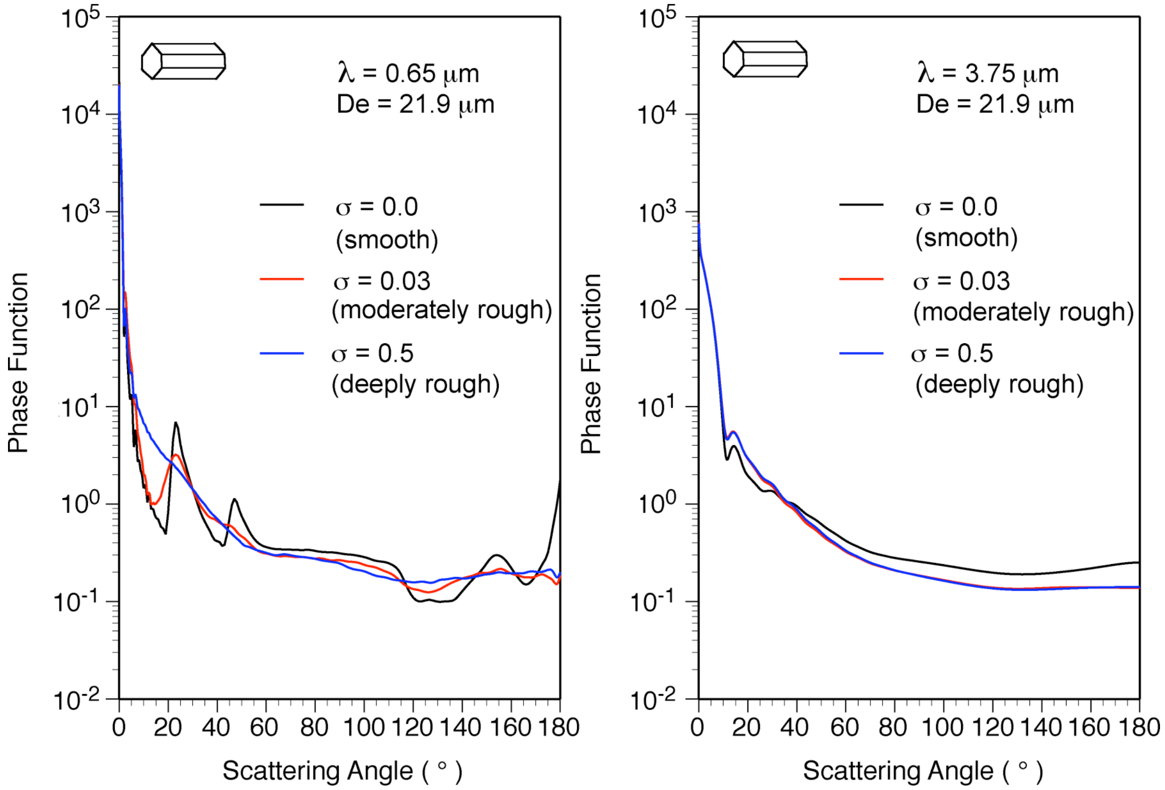

Fig. 5. Ice crystal bulk-scattering phase functions at λ=0.65 μm and λ=3.75 μm, De=21.9 μm.

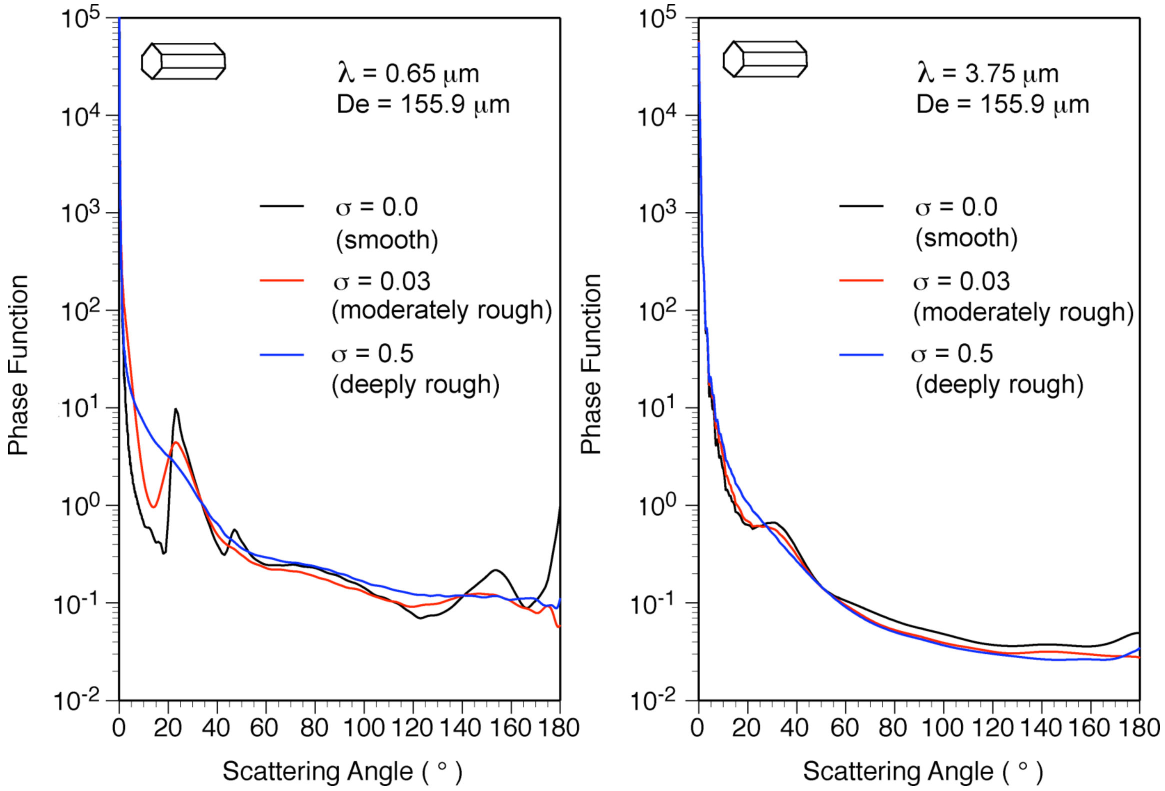

Fig. 6. Ice crystal bulk-scattering phase functions at λ=0.65 μm and λ=3.75 μm, De=155.9 μm

3.2 Ice cloud bidirectional reflectance

The bi-directional reflectance of ice cloud is computed by the DISORT model for λ = 0.65 μm and λ = 3.75 μm at φ = 0°, 2.5°, 5°, 10°, 15°, 25°, 35°, 45°, … , 165°, 170°, 175°, 177.5°, and 180° for the optical thickness τ = 0.25, 0.5, 1, 2, 3, 4, 8, 16, 32, 64, and 128. An array of solar and viewing zenith angles are also constructed using μ_o = 1.0, 0.95, 0.85, … , 0.0 and μ = 1.0, 0.95, 0.85, … , 0.0, where $\mu_o = \cos\theta_o$ and $\mu = \cos\theta$. The visible optical thickness at λ = 0.65 μm serves as the reference optical thickness in this study. The optical thickness for a given wavelength is related to the visible optical thickness by Eq. (16).

To understand how the particle surface roughness affects the radiative transfer process, the library of bi-directional reflectances was read from the parameterization of cloud reflectance for a variety of effective particle sizes and optical thickness, and a combination of μ_0=0.65, μ=1.0 and $\varphi - \varphi_0$ = 0°. The comparison of the lookup tables between smooth and moderately rough particles is shown in Fig. 7. The small-particle reflectances are typically greater than those for the larger particles of both roughness conditions. The vertical lines of reflectances with the same optical thickness indicate that the upwelling radiances have little sensitivity to effective particles sizes at λ=0.65 μm. The moderately rough particles reflect more than smooth particles at λ=0.65 μm because of the spreading of the rays in the back scattering direction for rough particles. With consistency of the case at λ=0.65 μm, reflectances for rough particles less than 10 μm exceed those of smooth particles at λ=3.75 μm. Conversely, the smooth particles larger than 10 μm typically produce greater reflectances than the rough particles at λ=3.75 μm because of generally smaller asymmetry factors for smooth particles.

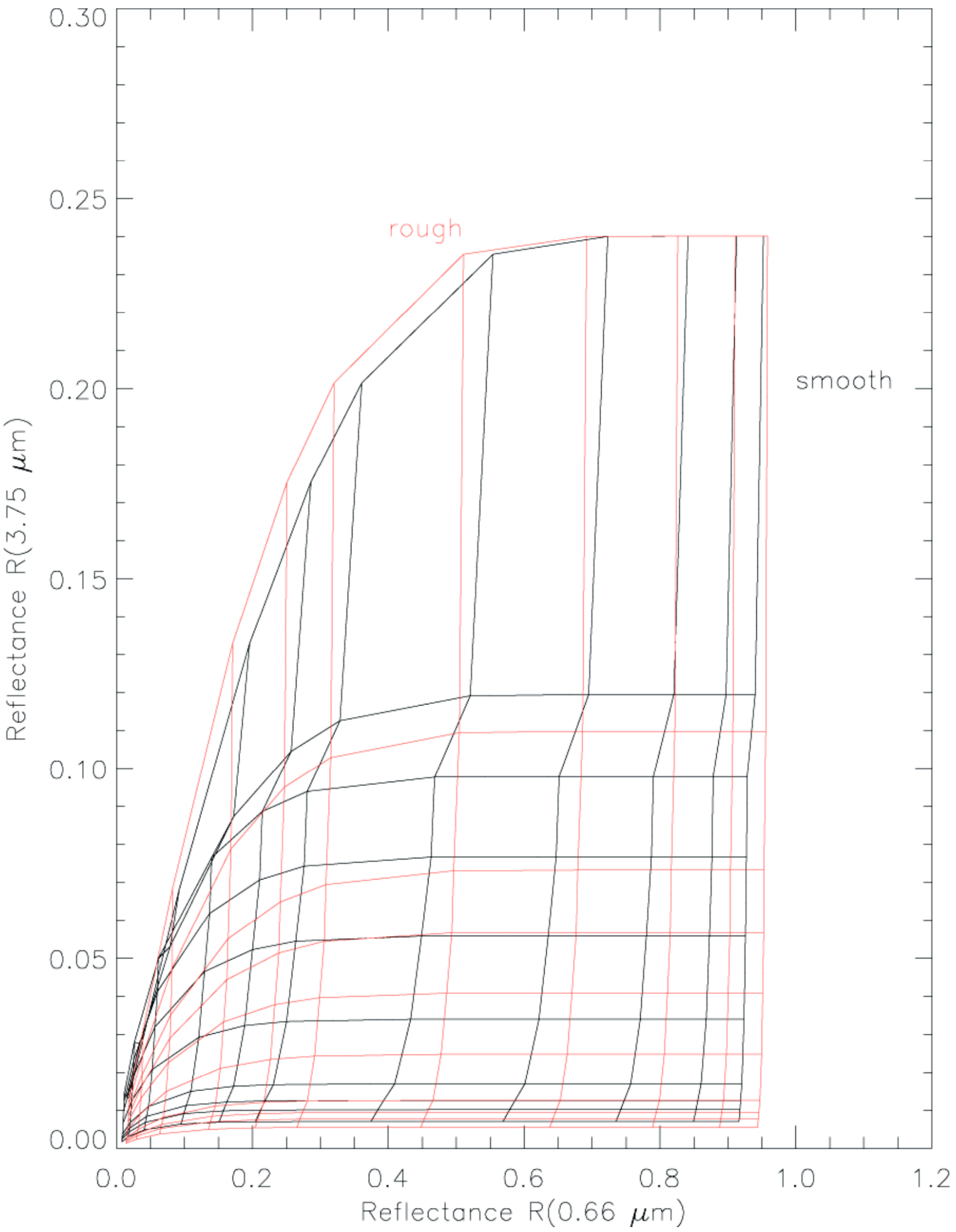

Fig. 7. Bidirectional reflectances from parameterizations for surface smooth and moderately rough particles at $\mu_o = 0.65$, $\mu = 1.0$, $\varphi - \varphi_o = 0°$

Figure 8 shows the ice cloud bidirectional reflectances for surface smooth, moderately rough and deeply rough particles at λ=0.65 μm, De=28.4 μm, μ_0=0.65, and cloud optical thickness τ=1.0. The patterns of the cloud bidirectional reflectances are similar for the three surface roughness conditions. It is seen in Fig. 8a that the relative maximum value of bidirectional reflectance appears at θ=85° and φ=0°. The relative minimum value is in a region for a variety of satellite viewing angles from θ=0° to 30°. Fig. 9 shows the differences of cloud bidirectional reflectance between surface moderately rough and smooth particles, and deeply rough and smooth particles. The patterns of the two panels in Fig. 9 conclud that the bidirectional reflectance increases with surface roughness in most of the viewing angles but may also decrease in some specific regions, e.g. θ=85° and φ=150°. The variation of bidirectional reflectance caused by the surface roughness increases with the surface becoming rougher, which is consistent with the single-scattering phase function in Fig 5. Similar patterns can also be found in Figs. 10 and 11, which are the same as Figs. 8 and 9, respectively, except that λ=3.75 μm.

3.3 Ice cloud effective emittance

The upwelling radiance over ice cloud is computed for λ = 3.75 μm, 10.8 μm and 11.9 μm; surface temperatures Ts = 240, 260, 280, 300, 320 K; ice cloud temperature Tc = 195, 210, … , 270 K; and μ = 1.0, 0.95, 0.85, … , 0.0. The optical thickness for these channels corresponding to the visible optical thickness τ = 0.25, 0.5, 1, 2, 3, 4, 8, 16, 32, 64, and 128 can be derived by employing Eq. (16). With a set of cloud-top temperatures,

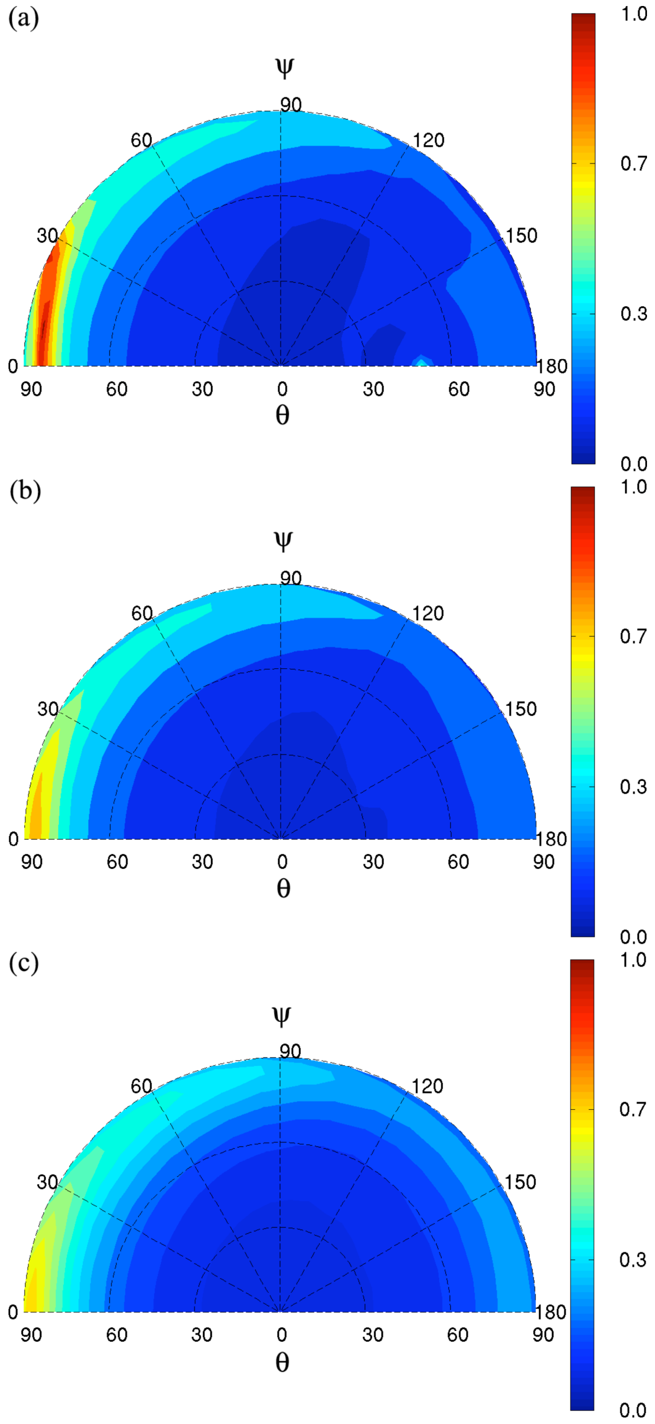

Fig. 8. Cloud bidirectional reflectances for (a) smooth, (b) moderately rough and (c) deeply rough particles at λ=0.65 μm, De=28.4 μm, μ_0=0.65, and τ=1.0.

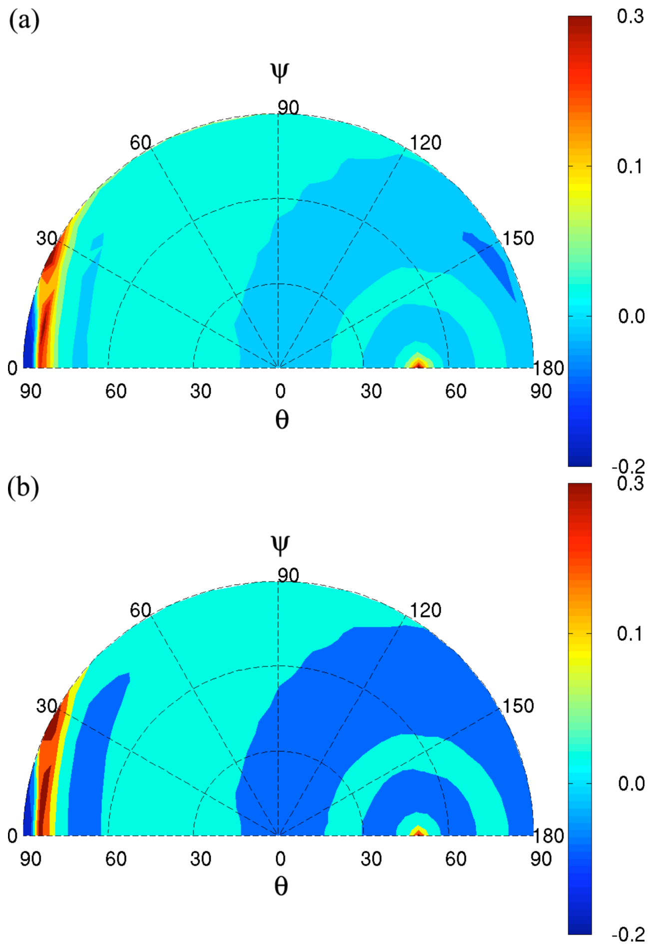

Fig. 9. Differences in cloud bidirectional reflectance between (a) moderately rough and smooth and (b) deeply rough and smooth particles at λ=0.65 μm, De=28.4 μm, μ_0=0.65, and τ=1.0.

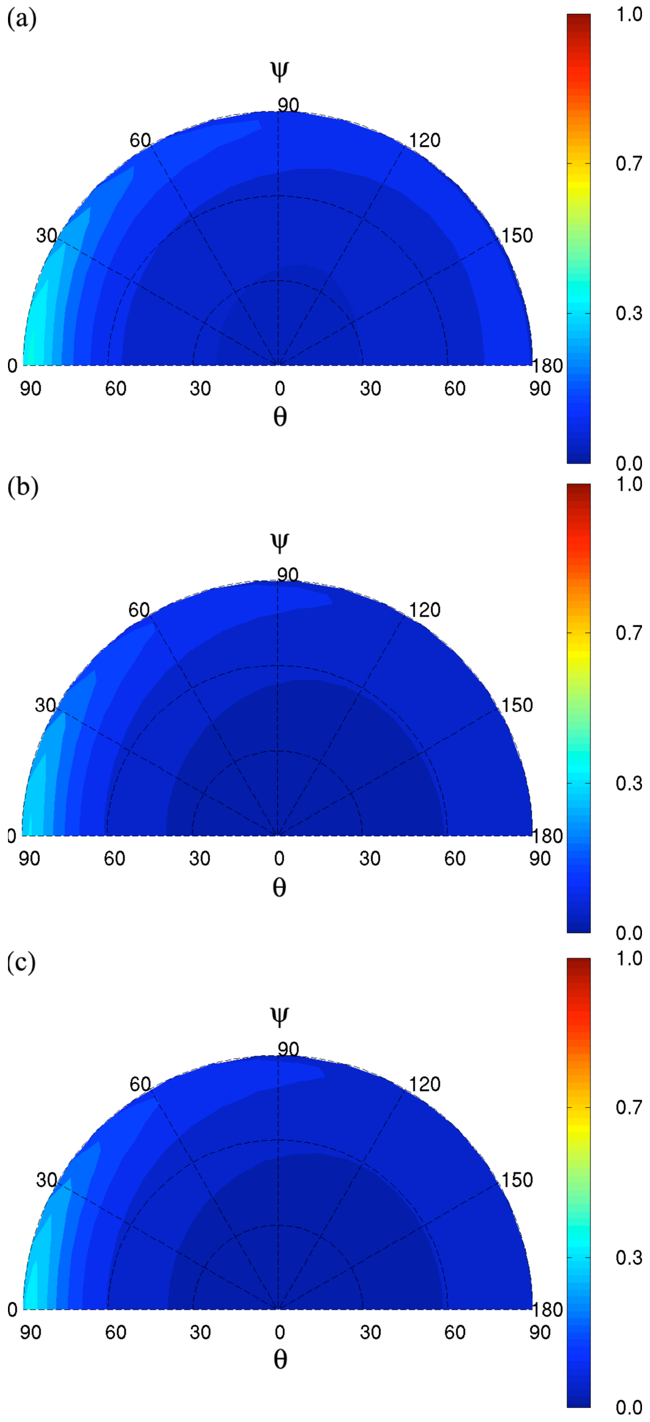

Fig. 10. Cloud bidirectional reflectances for (a) smooth, (b) moderately rough and (c) deeply rough particles at λ=3.75 μm, De=28.4 μm, μ_0=0.65, and τ=1.0.

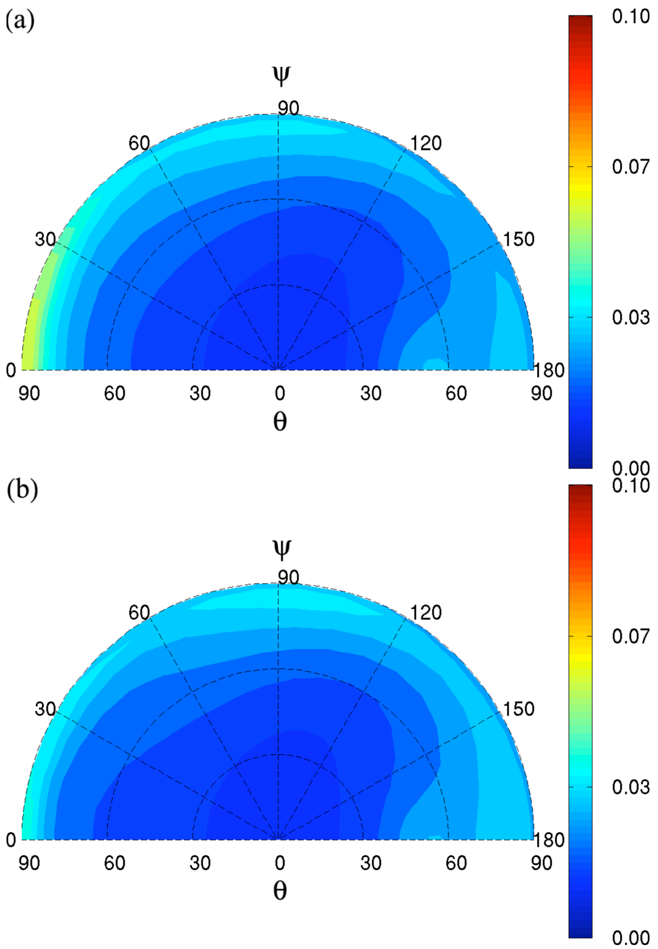

Fig. 11. Differences in cloud bidirectional reflectance between (a) moderately rough and smooth and (b) deeply rough and smooth particles at λ=3.75 μm, De=28.4 μm, μ_0=0.65, and τ=1.0.

surface temperatures, and simulated brightness at the TOA, the effective emittances for channel i is then parameterized from Eq. (7).

Figures 12 and 13 show the effective emittances for De = 46.33 μm at λ = 3.75 μm and 10.8 μm, respectively. The results fit very well with the parameterization model in Minnis et al. (1993), which is given by

$$\varepsilon = 1 - \exp[a(\tau/\mu)^b], \tag{24}$$

where τ is cloud optical thickness, a and b are regression coefficients. Figs. 14 and 15 show the effective emittances as a function of clear-cloud temperature differences for De = 46.33 μm at λ = 3.75 μm and 10.8 μm, respectively. Consistent with the discussion in Minnis et al. (1998), the effective emittances at 3.75 μm are larger because of greater scattering in that band. The patterns of Figs. 14 and 15 also have an apparent logarithmic dependence on clear-cloud temperature difference. So an error in the simulated effective emittance may minimally affect the retrieved cloud-top temperature which is one of the reasons that infrared wavelength is employed for deriving the cloud temperature. Figure 16 shows the brightness temperature differences (BTDs) from parameterizations for Ts = 300 K, Tc = 255 K, μ = 0.85. It is seen that the BTD increase when the effective particle size decreases, which indicates similar behavior for the variability of effective emittance.

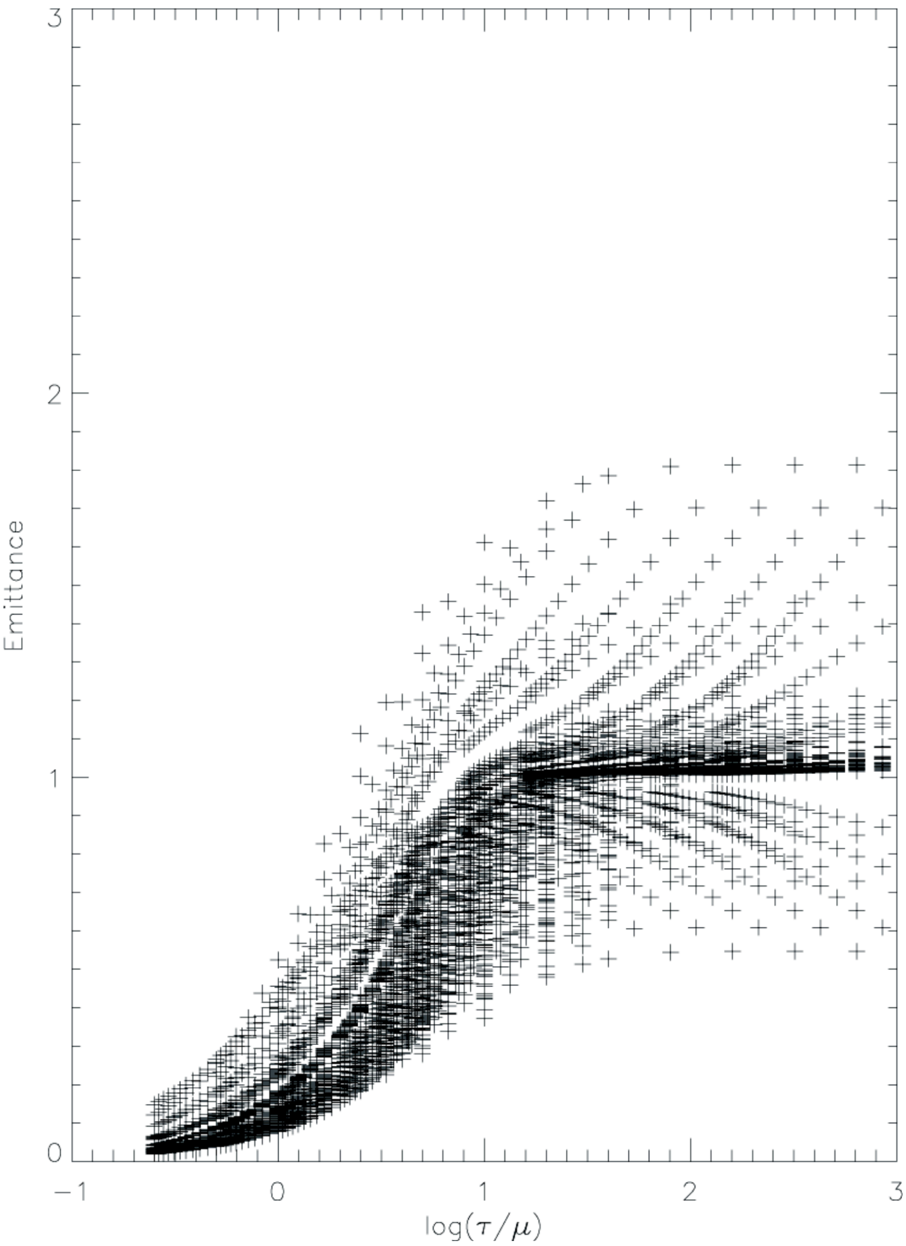

Fig. 12. Effective emittances for all calculations at λ=3.75 μm and De = 46.33 μm

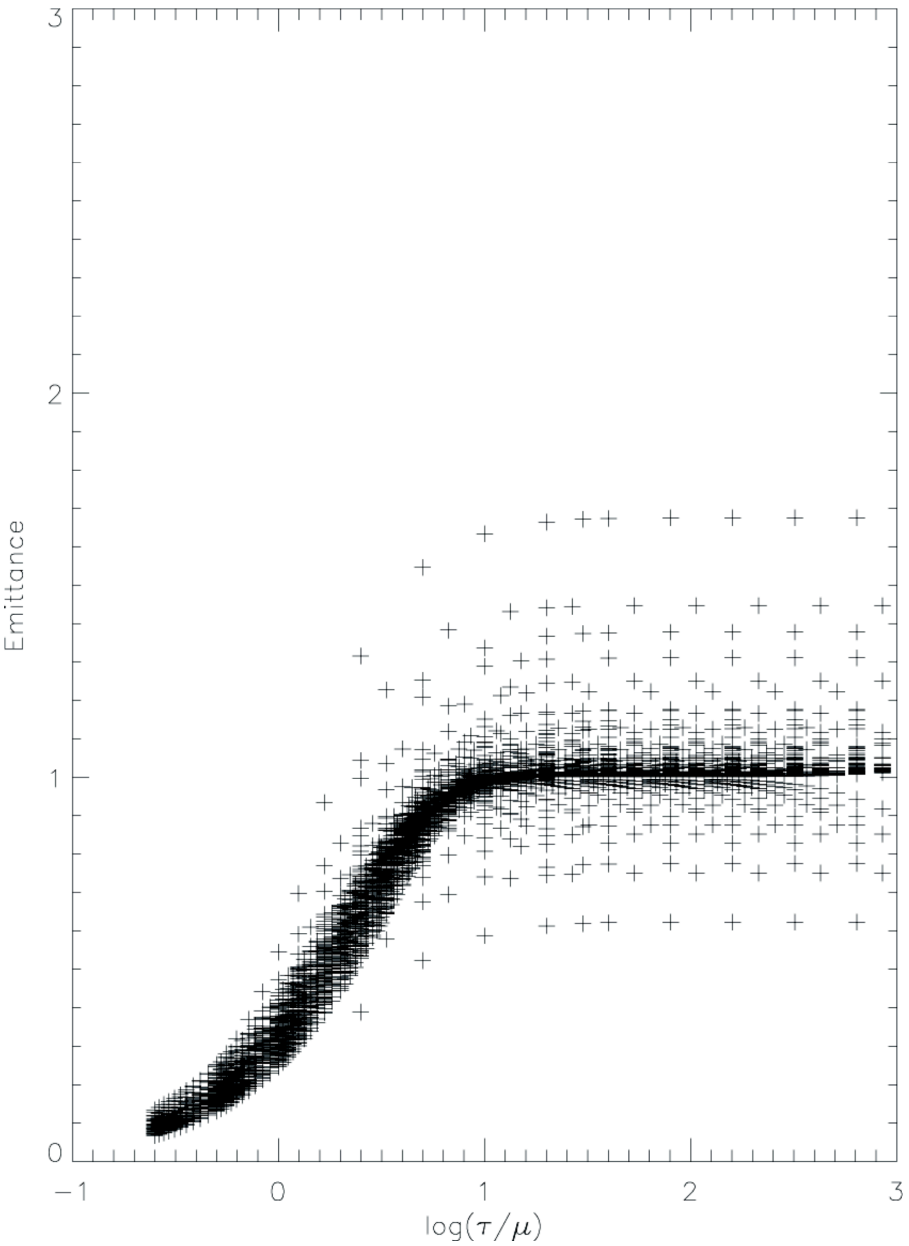

Fig. 13. Effective emittances for all calculations at λ=10.8 μm and De = 46.33 μm.

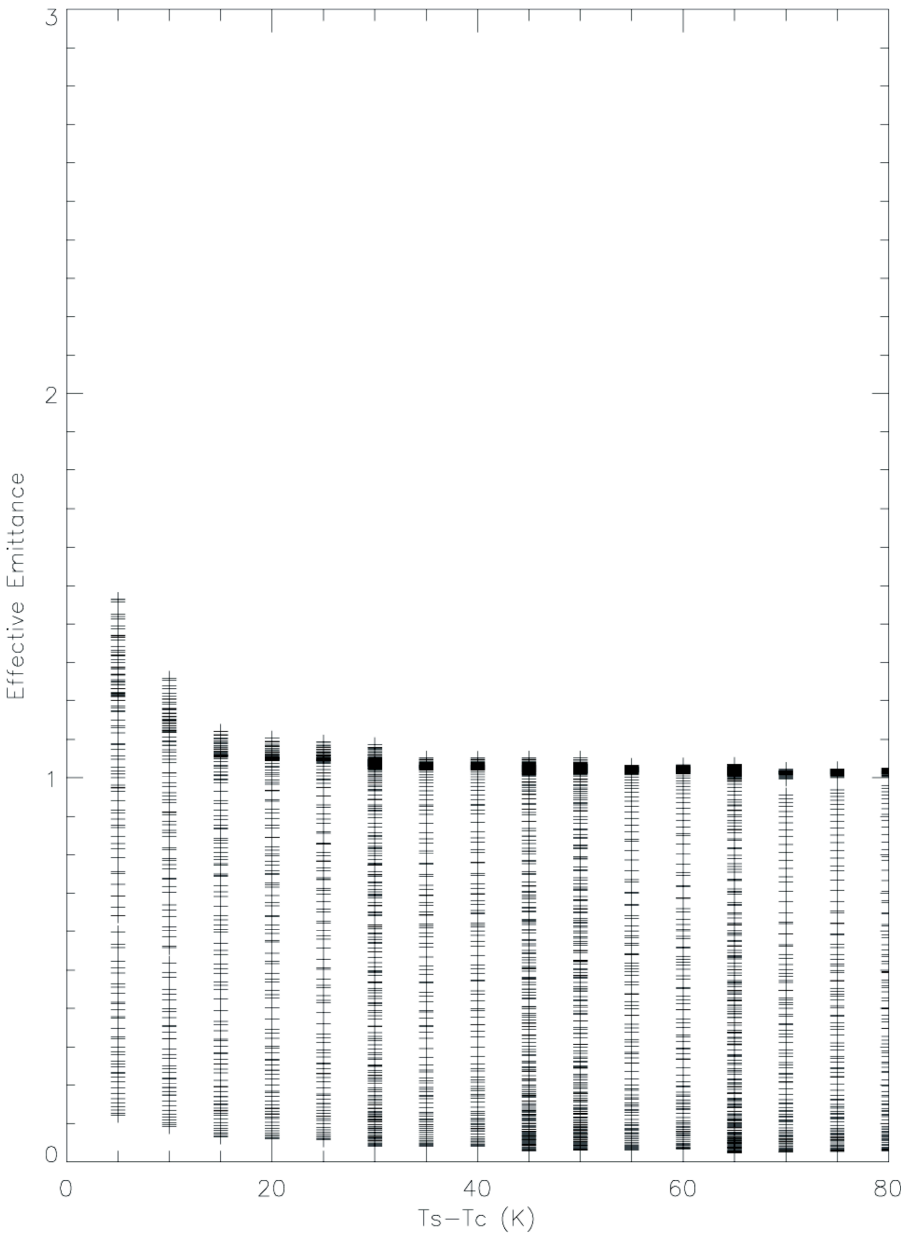

Fig. 14. Variation of effective emittance with clear-cloud temperature difference for λ = 3.75 μm and De = 46.33 μm.

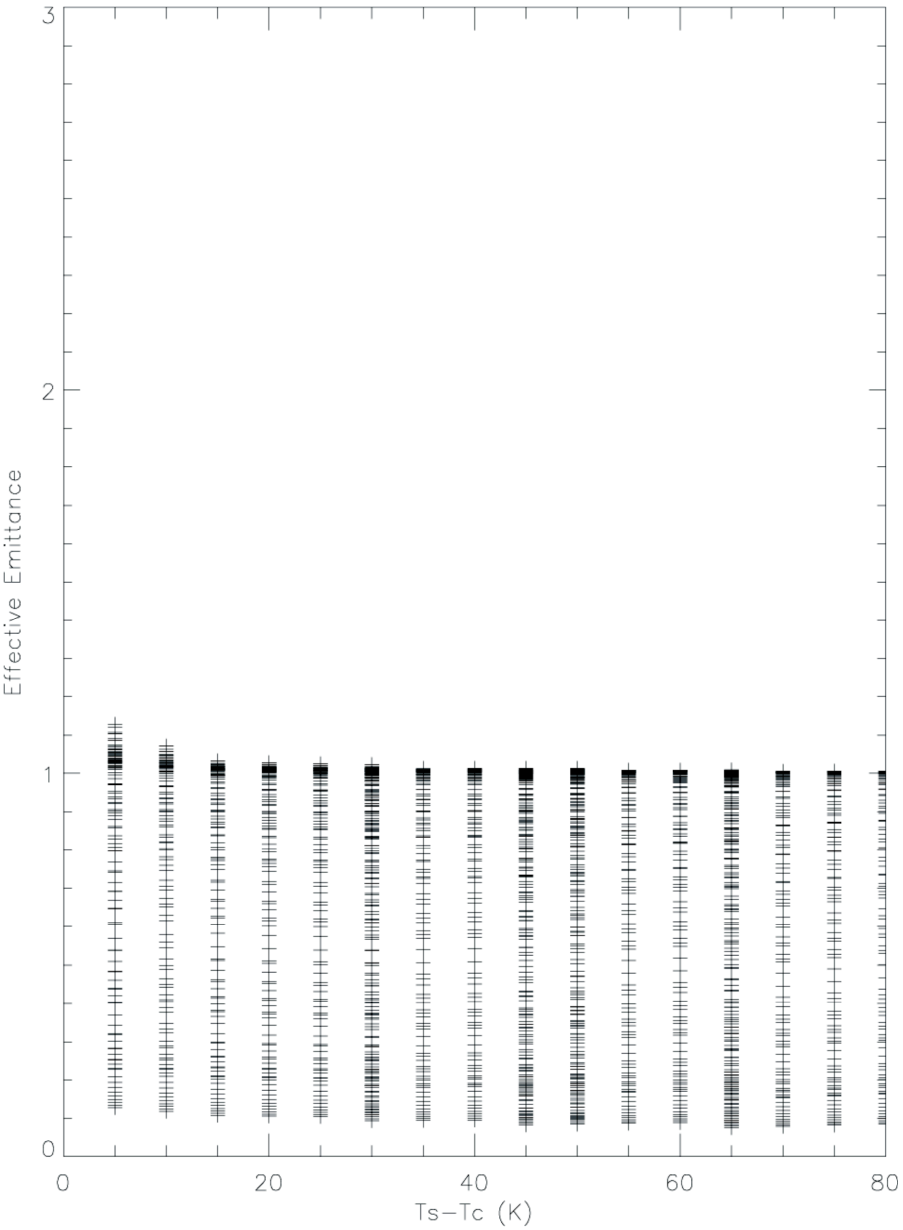

Fig. 15. Variation of effective emittance with clear-cloud temperature difference for λ = 10.8 μm and De = 46.33 μm.

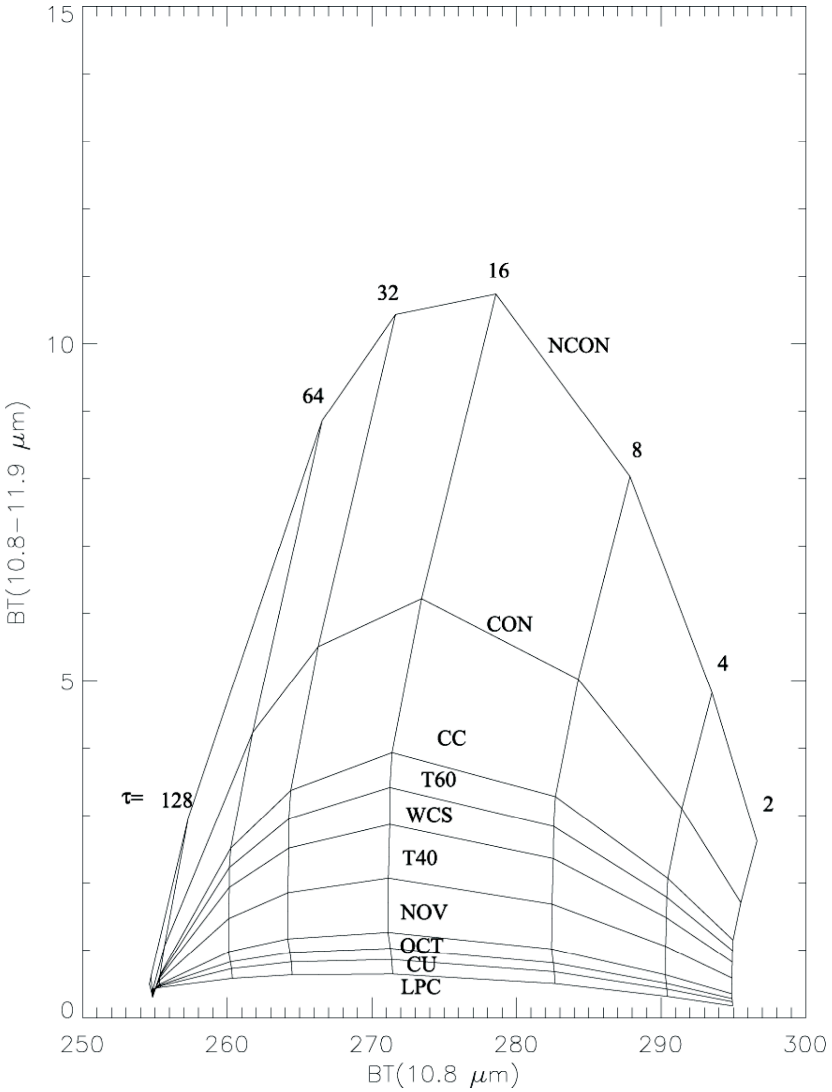

Fig. 16. Brightness temperature differences from parameterizations for Ts = 300 K, Tc = 255 K, μ = 0.85.

4. EFFECT OF ICE CRYSTAL SURFACE ROUGHNESS ON MODIS RETRIEVAL

To understand the effect of particle surface roughness on MODIS retrieval, two granules of retrieval using our 3-channel retrieval method are presented in this section.

4.1 Effect of ice crystal surface roughness on the retrieval of ice cloud microphysical and optical properties

Figures 17 and 18 show the MODIS image and cloud phase, respectively, over the South Atlantic Ocean observed on January 8, 2006. Retrieval results from MODIS are given in Figs. 19-27. Figure 19 shows the ice cloud effective particles size obtained by using surface smooth, moderately rough, and deeply rough particle models. The retrieved effective particle sizes vary from 10 to 90 μm. To indicate the effect of particle surface roughness on the retrieval of ice cloud particle size, Fig. 20 shows the subtractions of the effective particle sizes obtained by surface rough particles and those obtained by surface smooth particles. The effective particle sizes are significantly reduced by accounting for the surface roughness. It is also seen that the maximum value of the effective particle size differences between using surface smooth and rough particles is around 25 μm; that value appears in the region of effective particle sizes from 55 to 60 μm. Relatively small differences are found for the smallest and largest particles with effective particle size as 10 and 90 μm, respectively. Figure 21 shows the relative differences of ice cloud effective particle sizes between using surface smooth and moderately rough, and surface smooth and deeply rough particle models. The values of effective particle sizes may

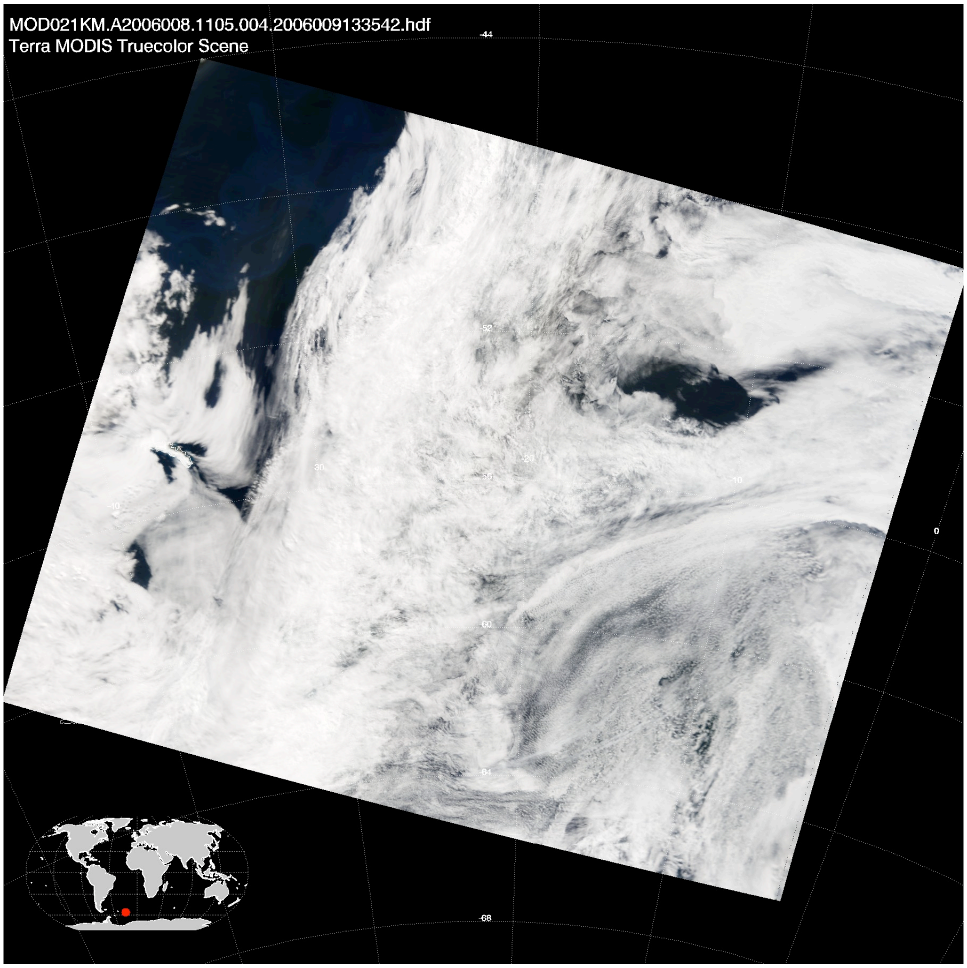

Fig. 17. Clouds over the South Atlantic Ocean observed with MODIS Level 1b data on January 8, 2006.

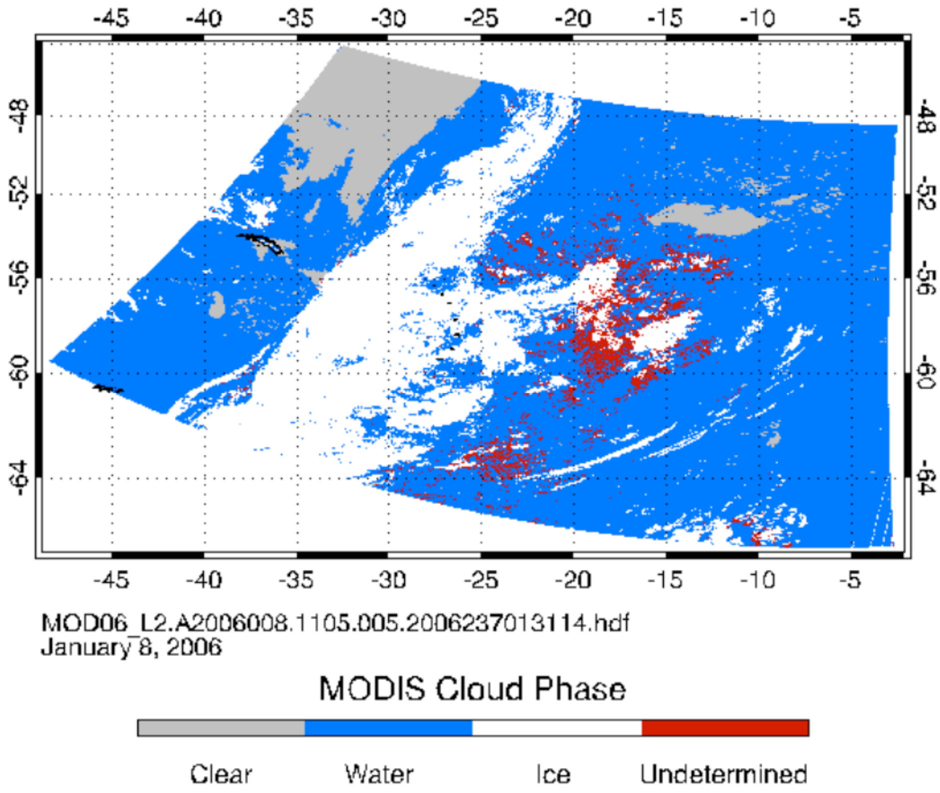

Fig. 18. MODIS cloud phase image for the granule shown in Figure 17.

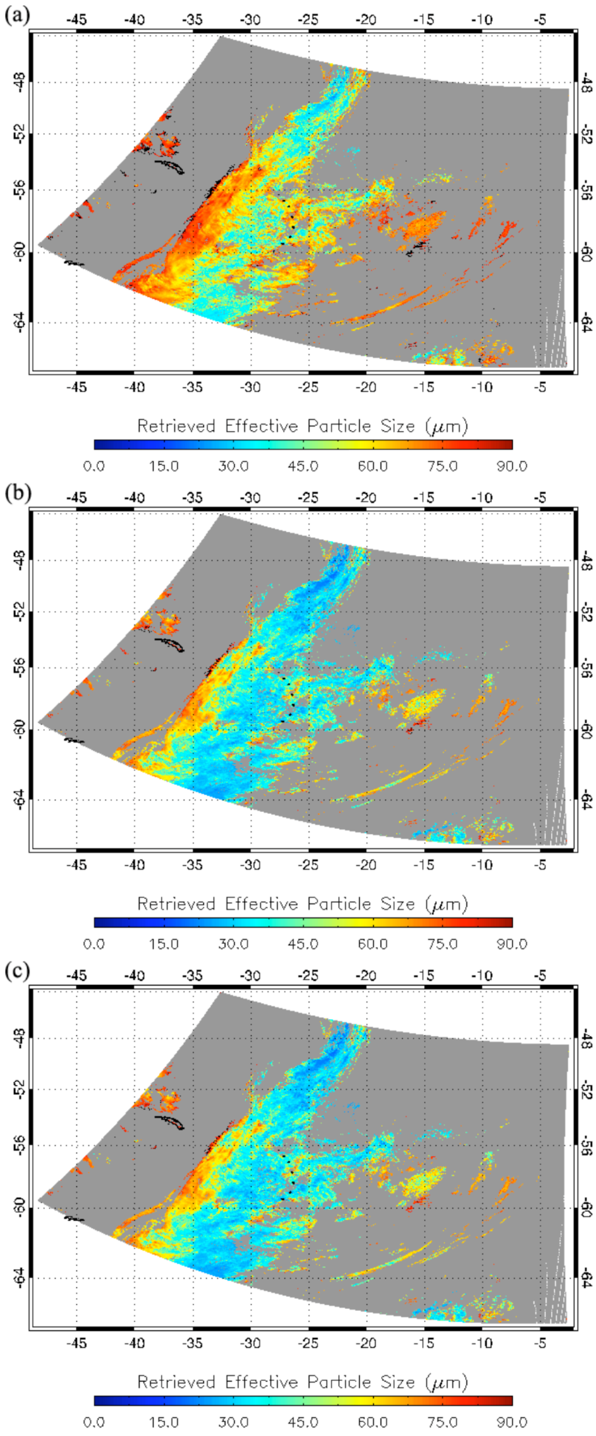

Fig. 19. Ice cloud effective particle sizes obtained by using (a) surface smooth, (b) moderately rough, and (c) deeply rough particle models.

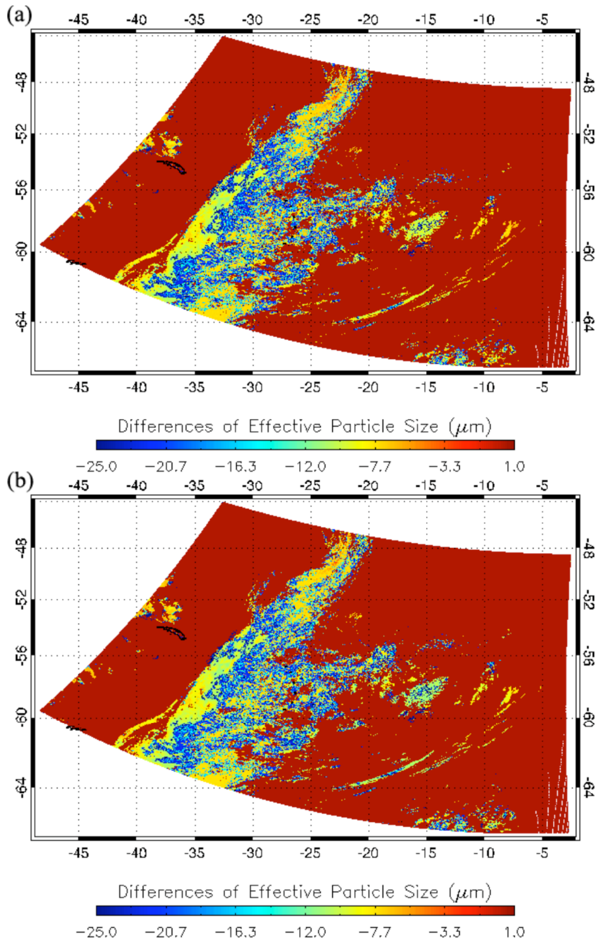

Fig. 20. Differences between ice cloud effective particle sizes using (a) surface smooth and moderately rough, and (b) surface smooth and deeply rough particle models.

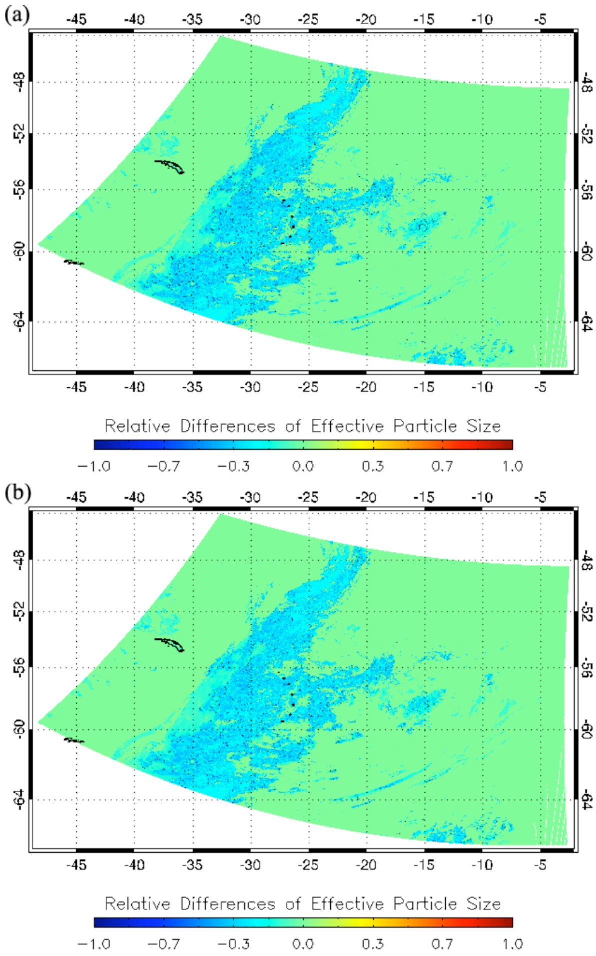

Fig. 21. Relative differences between ice cloud effective particle sizes using (a) surface smooth and moderately rough, and (b) surface smooth and deeply rough particle models.

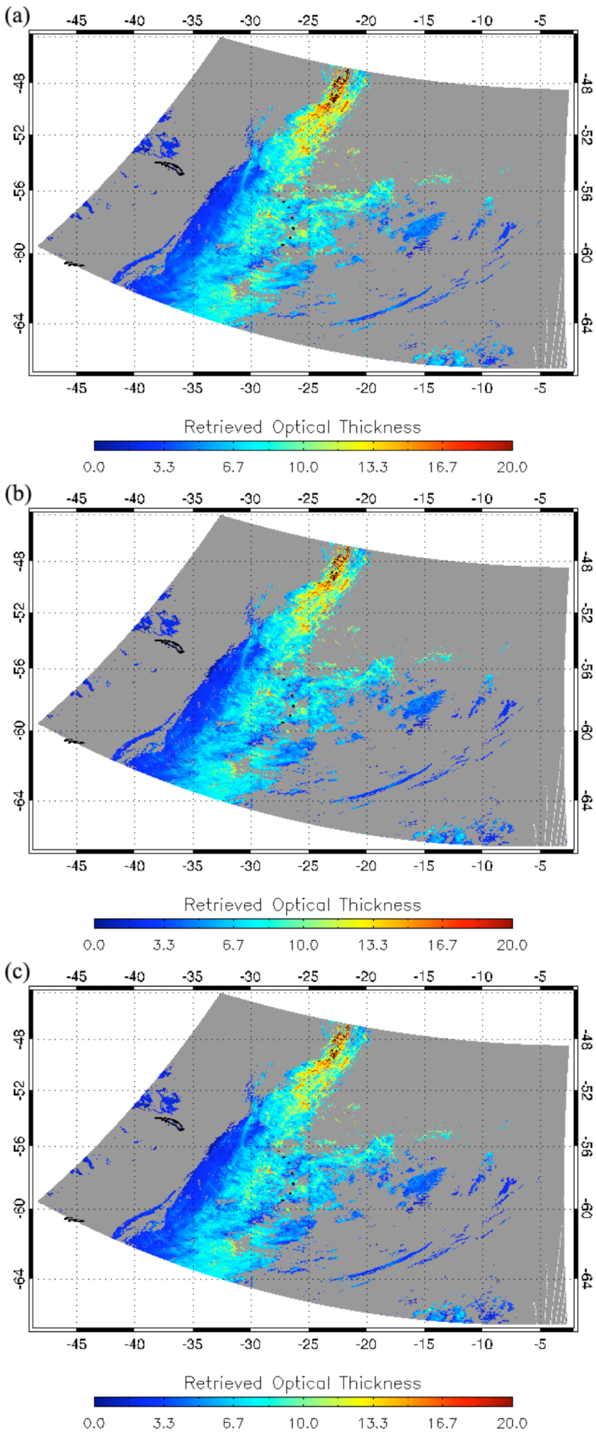

Fig. 22. Ice cloud optical thicknesses obtained by using (a) surface smooth, (b) moderately rough, and (c) deeply rough particle models.

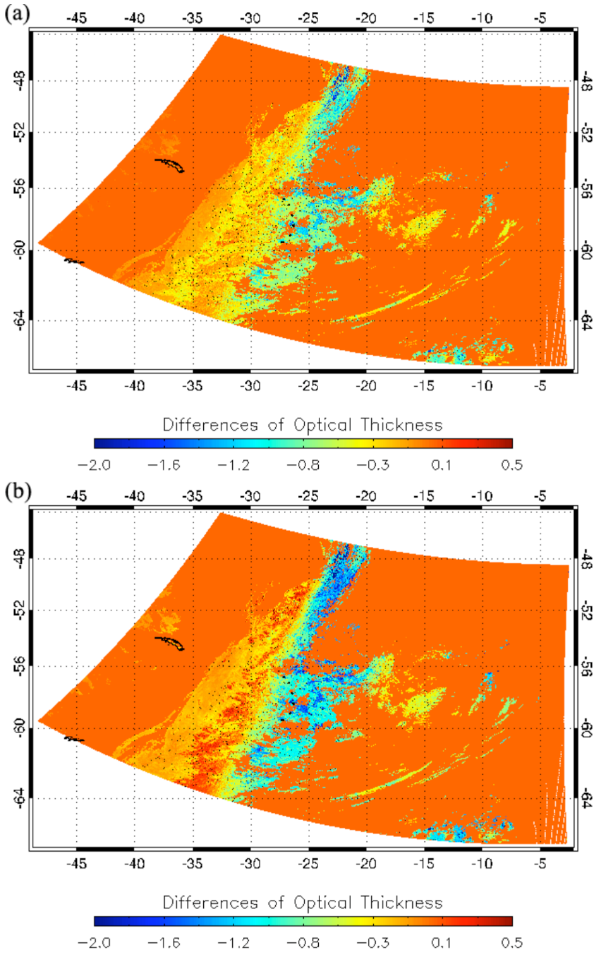

Fig. 23. Differences between ice cloud optical thicknesses using (a) surface smooth and moderately rough, and (b) surface smooth and deeply rough particle models.

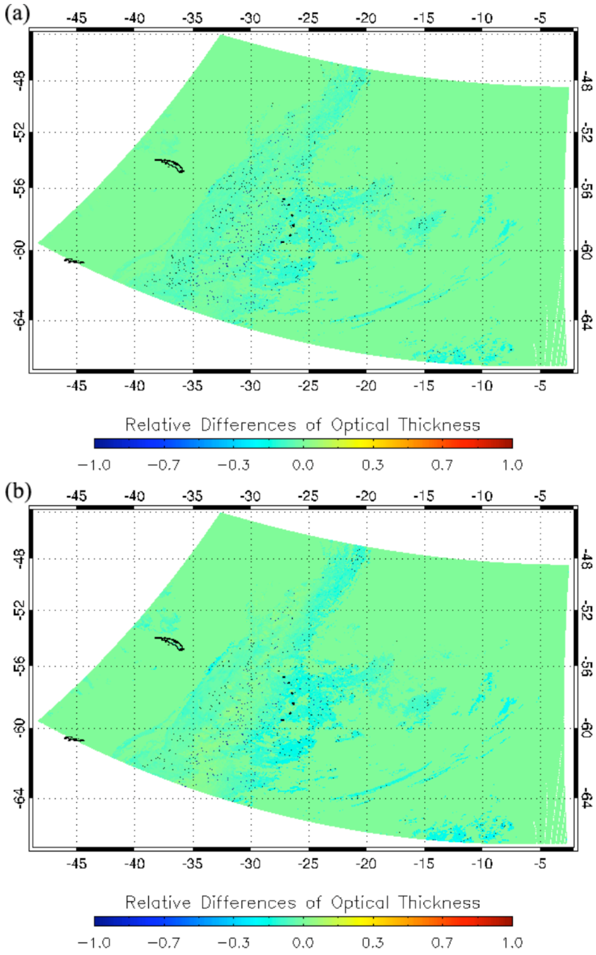

Fig. 24. Relative differences between ice cloud optical thicknesses using (a) surface smooth and moderately rough, and (b) surface smooth and deeply rough particle models.

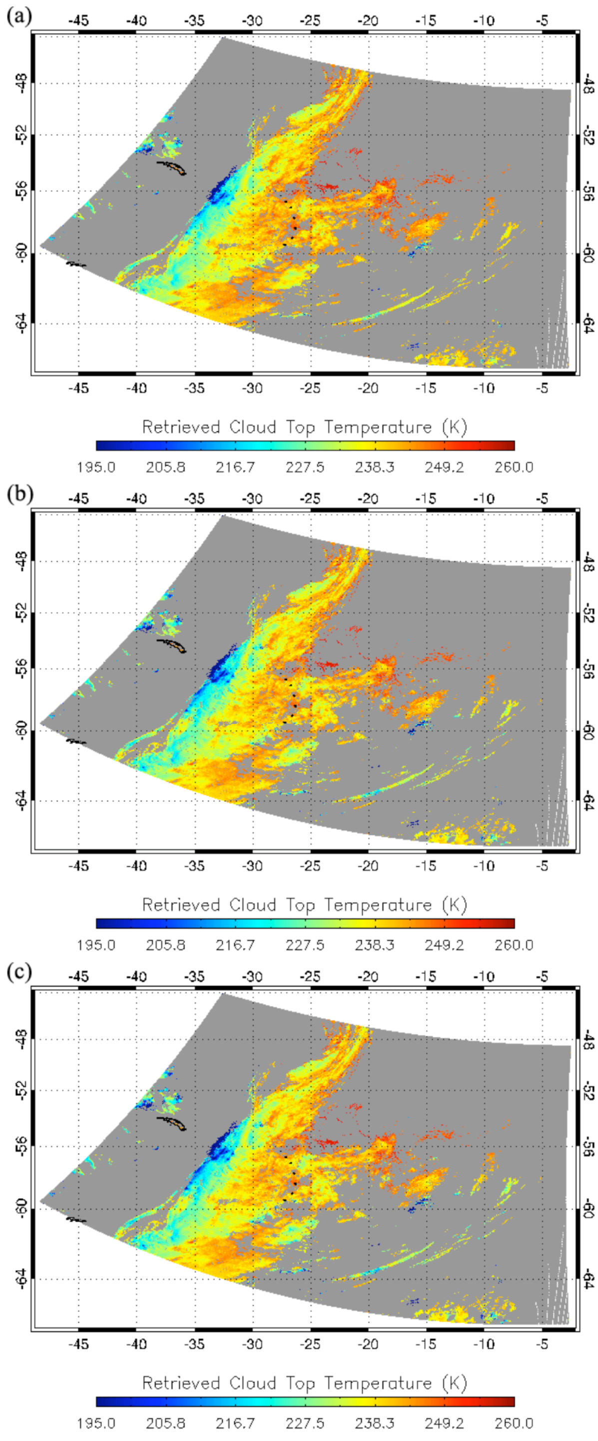

Fig. 25. Cloud-top temperatures obtained by using (a) surface smooth, (b) moderately rough, and (c) deeply rough particle models.

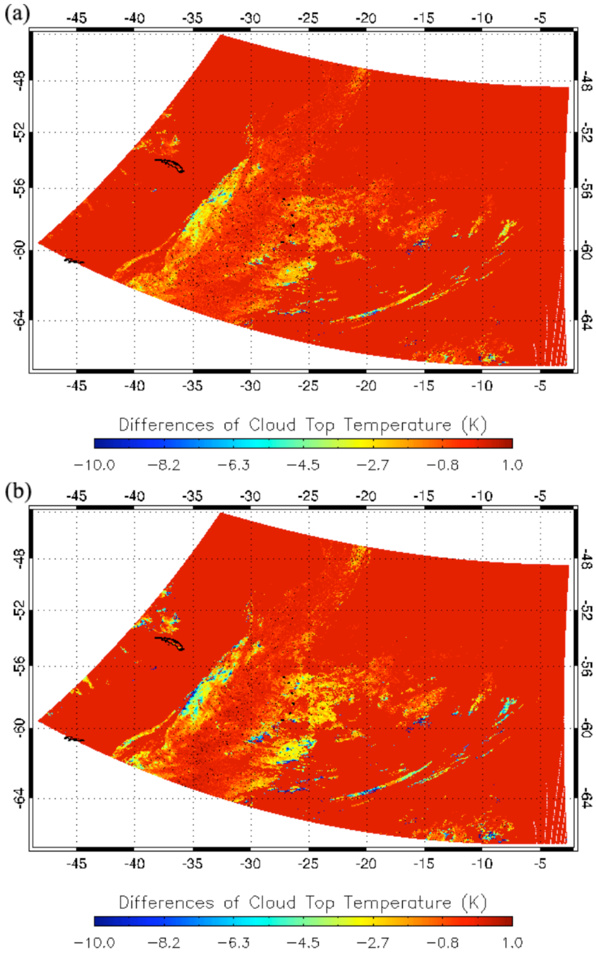

Fig. 26. Differences between cloud-top temperatures using (a) surface smooth and moderately rough, and (b) surface smooth and deeply rough particle models.

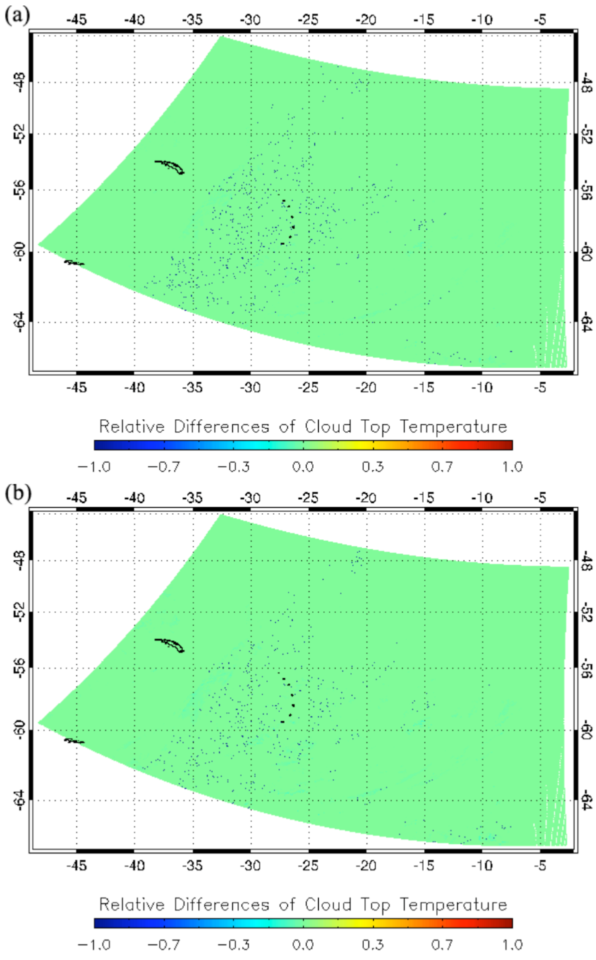

Fig. 27. Relative differences between cloud-top temperatures using (a) surface smooth and moderately rough, and (b) surface smooth and deeply rough particle models.

reduce from 20% to 40% by using surface rough particles. However, using moderately rough or deeply rough particles does not distinctly affect the retrieval of effective particle size. Figure 22 shows ice cloud optical thicknesses obtained by using surface smooth, moderately rough, and deeply rough particle models. It is indicated that optical thicknesses reduce more for the optically thick clouds in Figs. 23 and 24, which respectively show the optical thickness differences and relative differences between using surface smooth and moderately rough, and surface smooth and deeply rough particle models. Moreover, comparing Fig. 23a with Fig. 23b, the effect of surface roughness for the retrieval of cloud thick is more intensive if the particle surface becomes rougher. The typical relative differences of optical thicknesses are around 20% and 30%, respectively, for surface moderately rough and deeply rough particles. Figure 25 shows the cloud-top temperatures obtained by using the particle models with three different surface roughness conditions. The cloud-top temperatures for ice clouds shown in Fig. 17 are in a range of 195 to 250 K. It is then evident from Figs. 26 and 27, which illustrate the differences between cloud-top temperatures using surface smooth and rough particle models, that particle surface roughness has a very minor effect on the retrieval of cloud-top temperature because of the relatively small particle surface roughness compared with the long wavelength, which is used to derive cloud-top temperature.

Another study was performed on MODIS image located over the South Indian Ocean on January 11, 2005. Figures 28 and 29 show the MODIS cloud image and cloud phase for that granule, which has more ice cloud amount and larger ice cloud optical thickness compared with the MODIS data in Fig. 17. Figure 30 shows the ice cloud effective particle sizes retrieved by using the three surface roughness conditions. For the results from surface smooth particle models, the typical effective particle sizes are from 10 to 90 μm. Figures 31 and 32 respectively show the differences and relative differences between ice cloud effective particle sizes using surface smooth and moderately rough, and surface smooth and deeply rough particle models. Being consistent with Figs. 20 and 21, the maximum value of both the differences and relative differences appear on the effective particle sizes of around 60 μm. Again, the comparison of Figs. 31c and 31b presents minor effect of surface roughness on the retrieval of effective particle size. The retrieved ice cloud optical thicknesses, in Fig. 33, have a large variation from 0 to 30. Figure 34 shows the values of ice cloud optical thickness differences between using surface smooth and moderately rough, and surface smooth and deeply rough particle models. Similarly, with the results in Fig. 23, the retrieval by using surface roughness particle models significantly reduces the optical thickness in most of the pixels, especially for those with optically thick clouds. This effect becomes more impressive with the increasing of the surface roughness. However, some converted results are seen in a few small areas of Fig. 34 and 35. In those areas, e.g. in a region located in the center of latitude -50, longitude 142, the retrieved optical thickness slightly increases if the surface rough particle model is employed. Moreover, the results in those areas are getting to be even smaller with the deeper rough particle models being used in the retrieval. This would be related to both the cloud effective particles sizes and the cloud-top temperatures of those regions. Figure 36 shows the cloud-top temperatures obtained by using surface smooth, moderately rough and deeply rough particle models. It can be determined from Figs. 33 and 36 that the increased optical thickness in Fig. 34 is associated with the relatively large cloud optical thickness of around 18 and the high cloud-top temperature

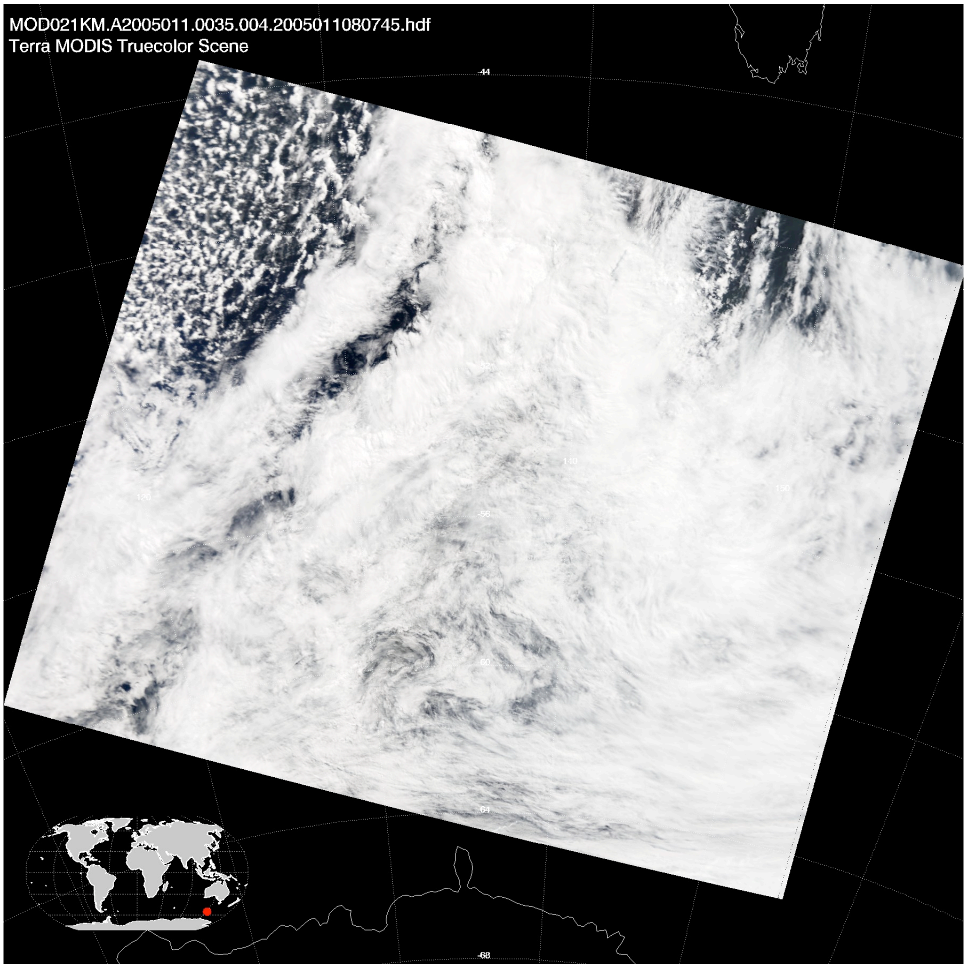

Fig. 28. Ice clouds over the South Indian Ocean observed with MODIS Level 1b data on January 11, 2005.

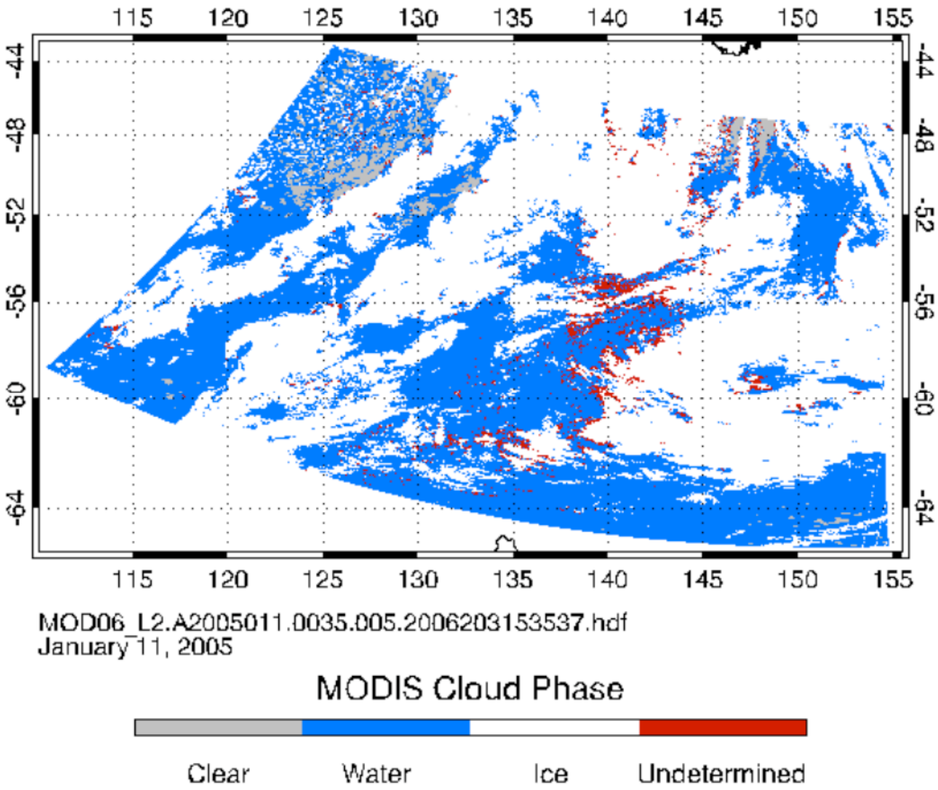

Fig. 29. MODIS cloud phase image for the granule shown in Fig. 28.

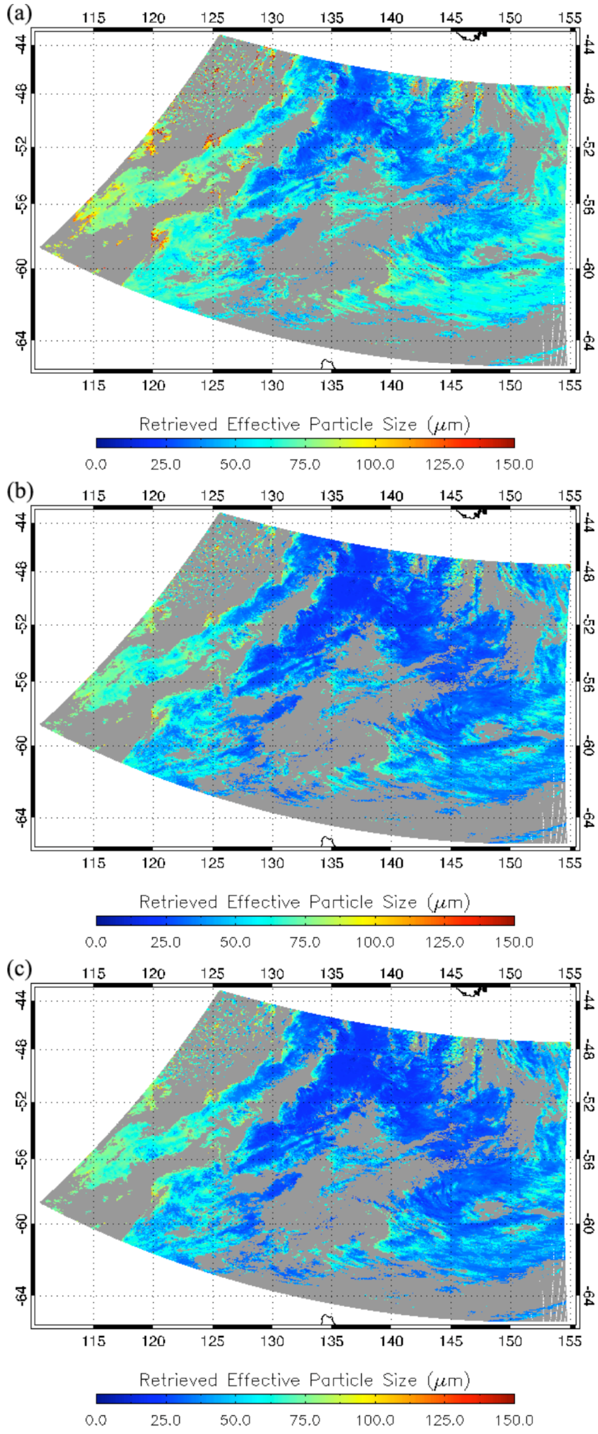

Fig. 30. Ice cloud effective particle sizes obtained by using (a) surface smooth, (b) moderately rough, and (c) deeply rough particle models.

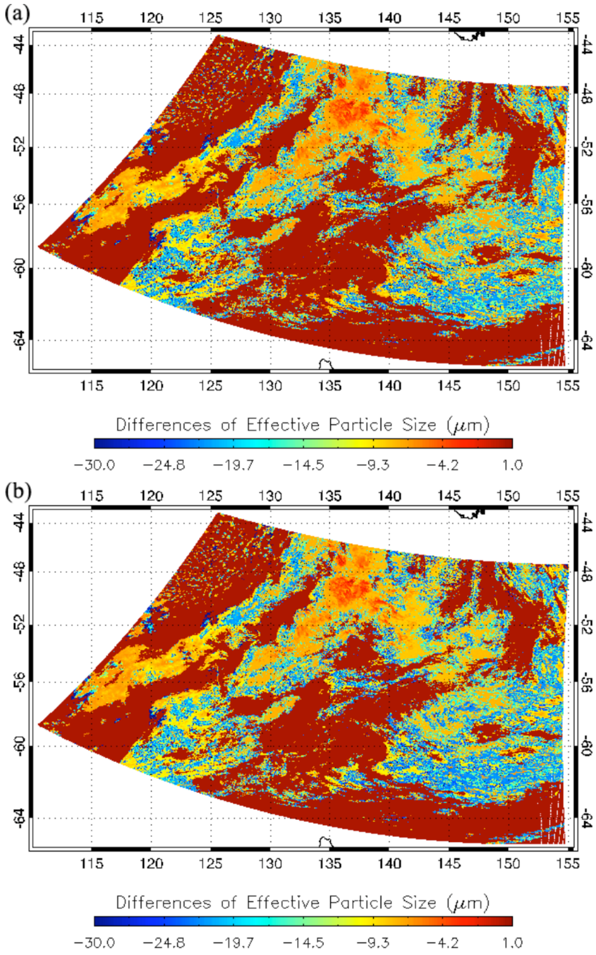

Fig. 31. Differences between ice cloud effective particle sizes using (a) surface smooth and moderately rough, and (b) surface smooth and deeply rough particle models.

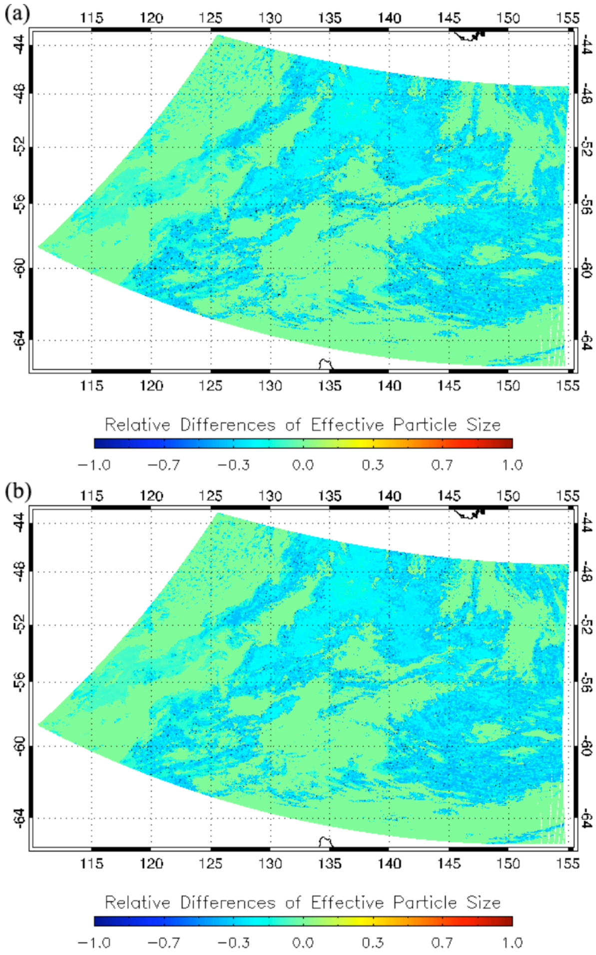

Fig. 32. Relative differences between ice cloud effective particle sizes using (a) surface smooth and moderately rough, and (b) surface smooth and deeply rough particle models.

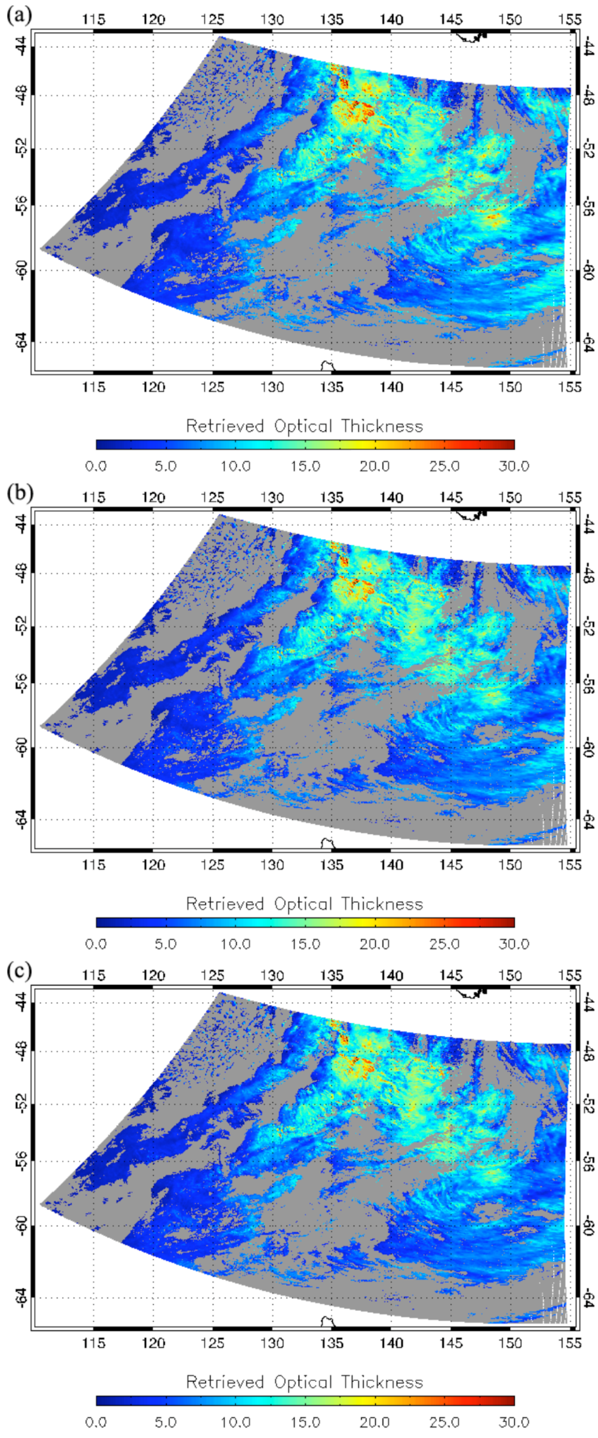

Fig. 33. Ice cloud optical thicknesses obtained by using (a) surface smooth, (b) moderately rough, and (c) deeply rough particle models.

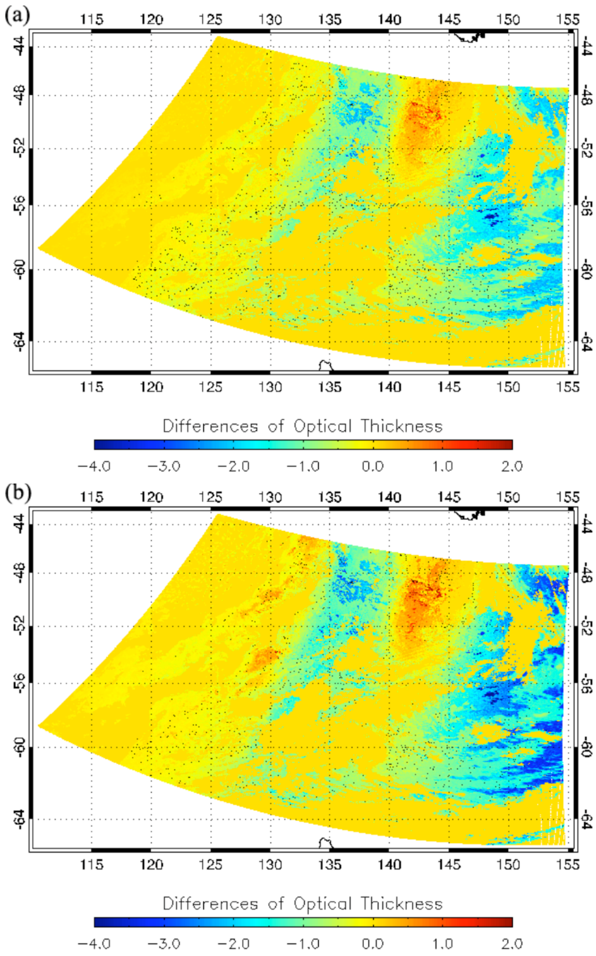

Fig. 34. Differences between ice cloud optical thicknesses using (a) surface smooth and moderately rough, and (b) surface smooth and deeply rough particle models.

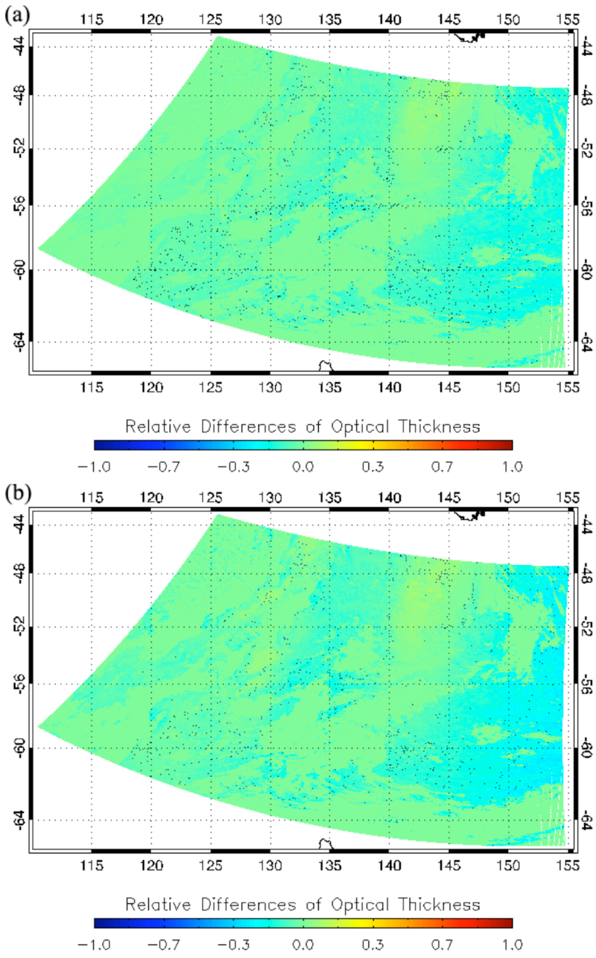

Fig. 35. Relative differences between ice cloud optical thicknesses using (a) surface smooth and moderately rough, and (b) surface smooth and deeply rough particle models.

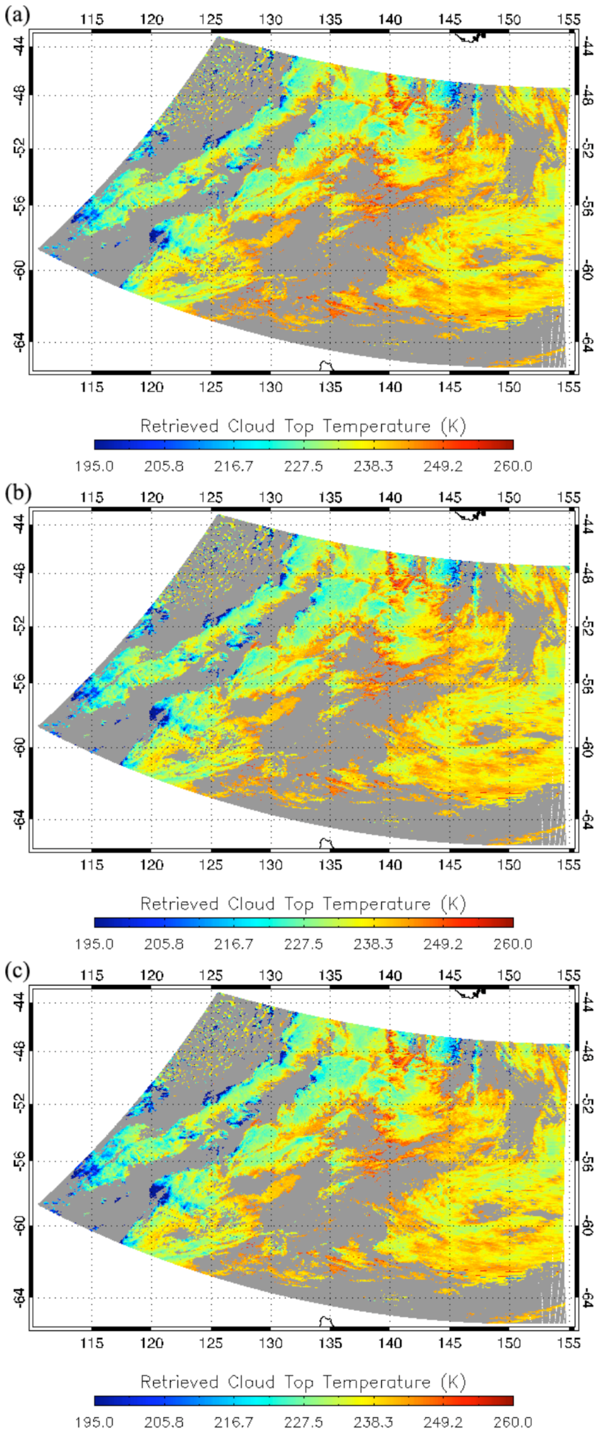

Fig. 36. Cloud-top temperatures obtained by using (a) surface smooth, (b) moderately rough, and (c) deeply rough particle models.

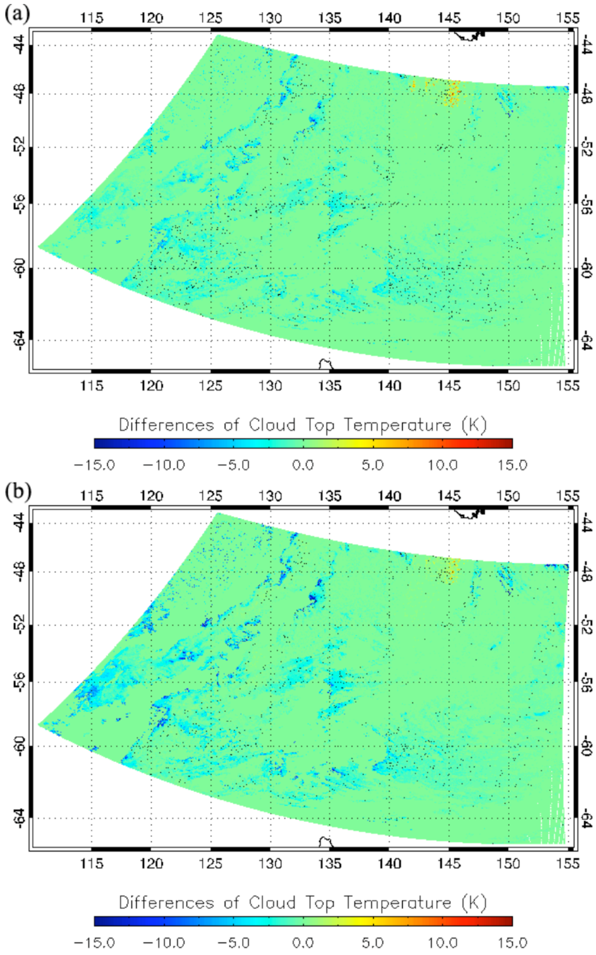

Fig. 37. Differences between cloud-top temperatures using (a) surface smooth and moderately rough, and (b) surface smooth and deeply rough particle models.

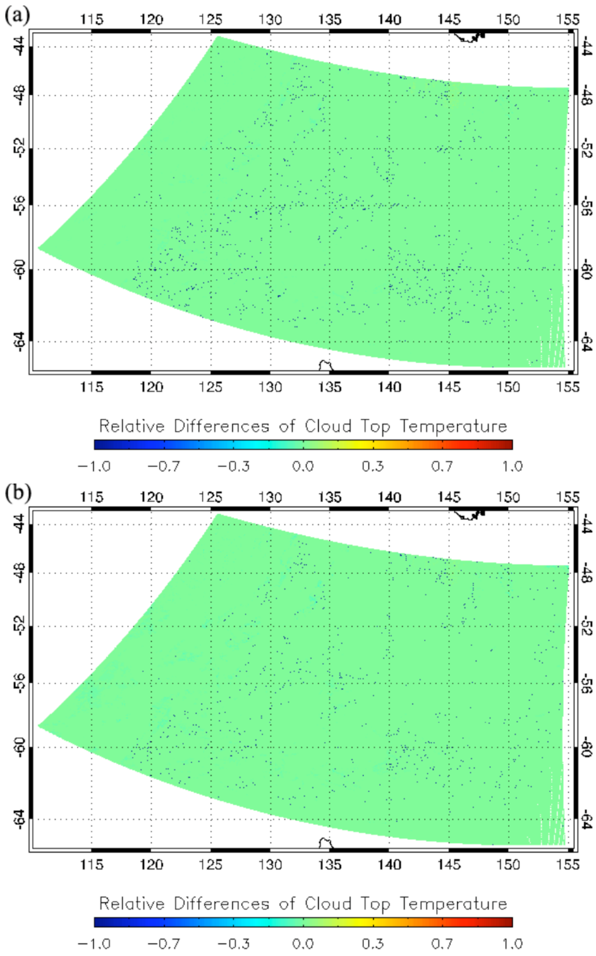

Fig. 38. Relative differences between cloud-top temperatures using (a) surface smooth and moderately rough, and (b) surface smooth and deeply rough particle models.

of around 240 K. Figure 37 shows the differences between cloud-top temperatures using surface smooth and moderately rough, and surface smooth and deeply rough particle models. The maximum reduction of cloud-top temperature using surface rough particles is around 15 K. However, this value is relatively small if divided by cloud-top temperature in Fig. 38, which shows the relative differences of cloud-top temperatures between using surface smooth and moderately rough, and surface smooth and deeply rough particles models. A few black spots in Fig. 38 indicate that some of the retrieved pixels may have retrieval results by employing surface smooth particles but not if employing surface rough particles. Or conversely, some pixels may get values for using surface rough particle models while there is no retrieval possible in the analysis system with surface smooth particle models.

4.2 Distributions of the retrieval results

Figure 39 shows the histograms of the ice cloud effective particle sizes, and the differences and relative differences between ice cloud effective particle sizes using surface smooth and deeply rough particle models for the MODIS granule in Fig. 17. Figure 39a illustrates that the retrieved effective particles are most frequently found around 30 and 60 μm while there is an absence of effective particle size of 50 μm. According to the discussion above, the retrieval using surface rough particles may cause an underestimate of effective particle size. However, over 50% of the results have slight reductions within 15 μm, which can be found in Fig. 39b. Another peak of effective particle size reduction distribution of the histogram in Fig. 39b is at 20 to 25 μm. Although the reductions in most of the effective particle sizes are small, the common

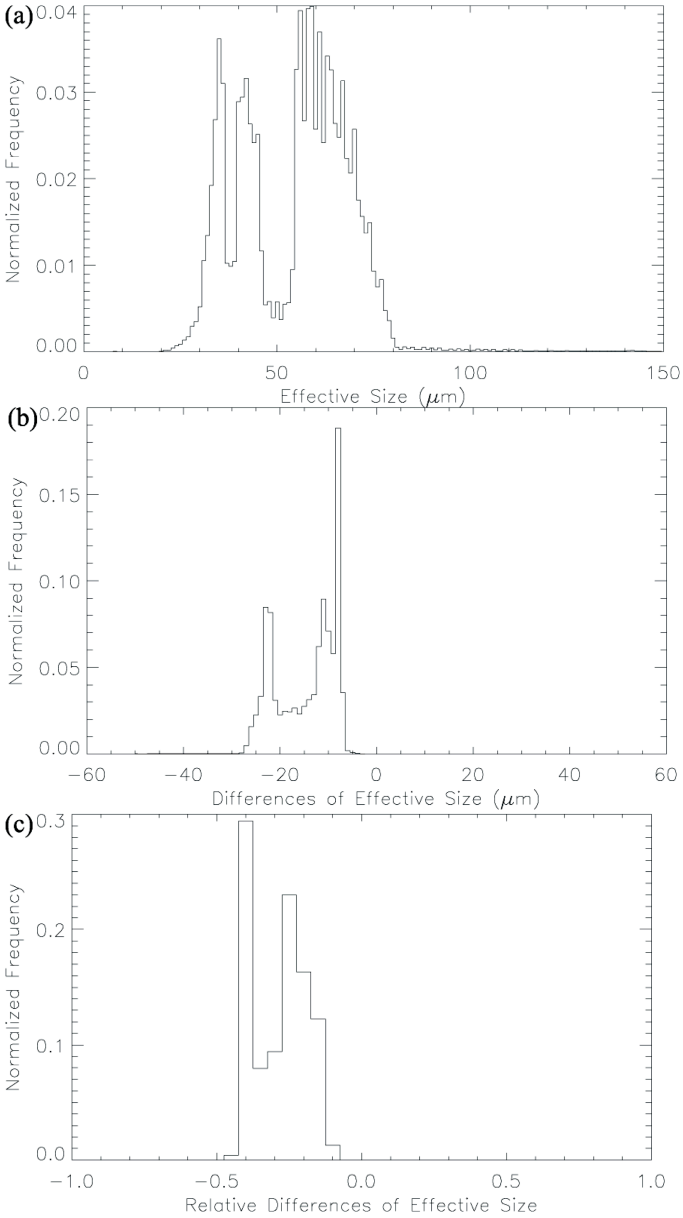

Fig. 39. Histograms of (a) ice cloud effective particle sizes, (b) differences between ice cloud effective particle sizes using surface smooth and deeply rough particle models, (c) relative differences between ice cloud effective particle sizes using surface smooth and deeply rough particle models for the MODIS granule shown in Fig. 17.

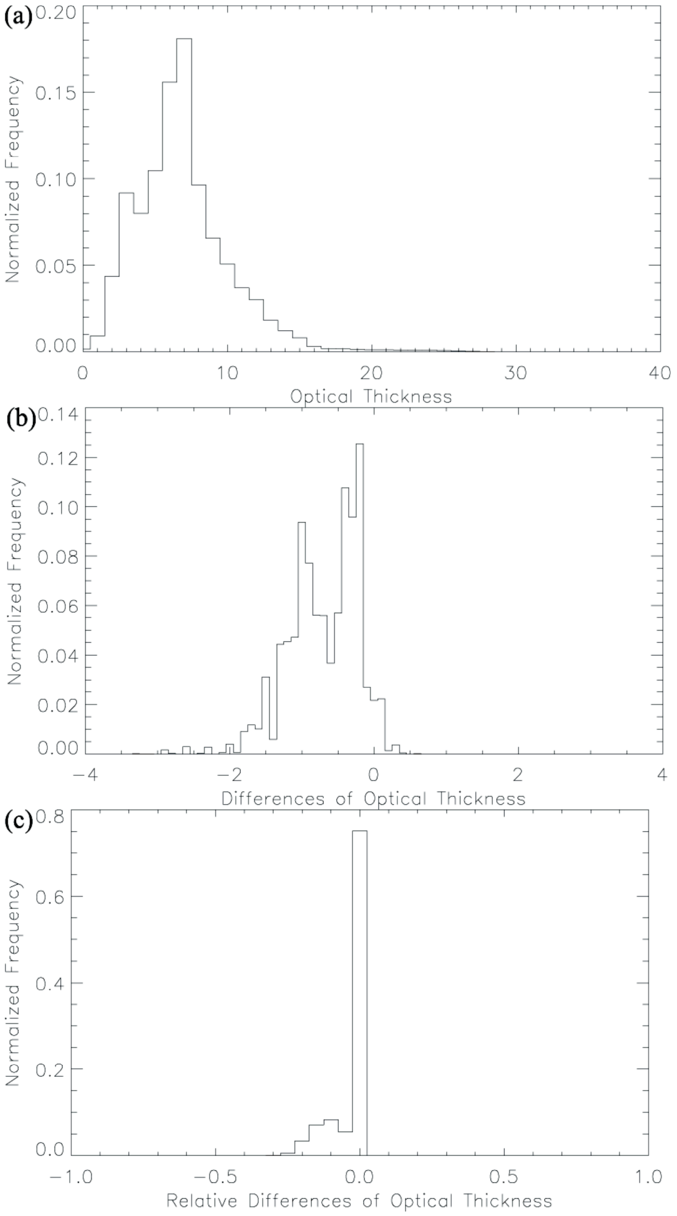

Fig. 40. Histograms of (a) ice cloud optical thicknesses, (b) differences between ice cloud optical thicknesses using surface smooth and deeply rough particle models, (c) relative differences between ice cloud optical thicknesses using surface smooth and deeply rough particle models for the MODIS granule shown in Fig. 17.

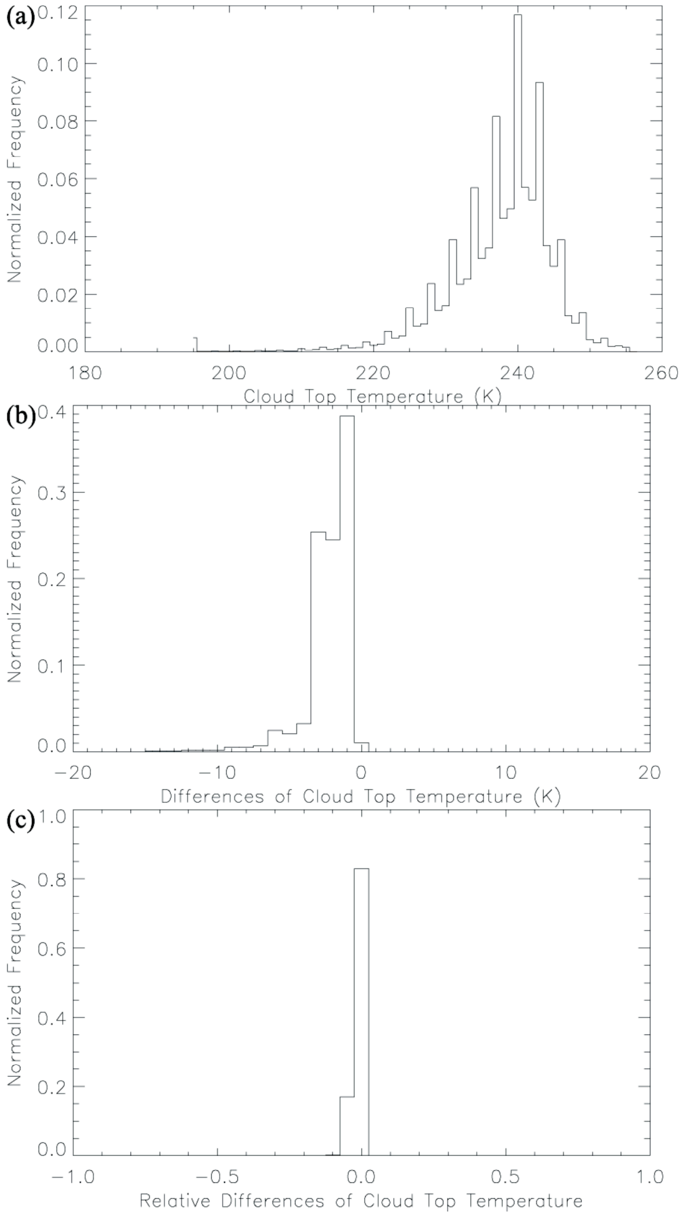

Fig. 41. Histograms of (a) cloud-top temperatures, (b) differences between cloud-top temperatures using surface smooth and deeply rough particle models, (c) relative differences between cloud-top temperatures using surface smooth and deeply rough particle models for the MODIS granule shown in Fig. 17.

values of the relative differences of effective particle sizes in Fig. 39c are as large as 40%. That means many small particles make relatively large reductions by using surface rough particle models.

Figure 40 shows the histograms of ice cloud optical thicknesses, and the differences and relative differences between ice cloud optical thicknesses using surface smooth and deeply rough particle models for the MODIS granule in Fig. 17. The average and most frequent value of retrieved optical thickness in Fig. 40a is around 5. Similarly, as the distribution for the reductions of effective particle sizes, the reductions of optical in Fig. 40b also have two peaks at 0.5 and 1. But the distribution of relative differences in Fig. 40c illustrates that around 80% of the pixels retrieved have no pronounced reductions.

Figure 41 shows the histograms of the cloud-top temperatures, and the differences and relative differences between cloud-top temperatures using surface smooth and deeply rough particle models for the MODIS granule in Fig. 17. The retrieved cloud-top temperatures have a variation from 195 to 260 K where the maximum value for the probability of density appears at 240 K. Consistent with the aforementioned discussion about cloud-top temperatures, the differences and relative differences of cloud-top temperatures, which are caused by using different surface roughness conditions, are concentrated at minor values in Figs. 41b and 41c, respectively.

Figures 42-44 show the histograms of effective particle sizes, optical thicknesses, and cloud-top temperatures, respectively, for MODIS granule shown in Fig. 28. Figure 42 shows the same pattern with Fig. 39 except that less probability of density is seen at 40% for the effective size relative differences in Fig. 42c. It is seen from Fig. 43a that the

MODIS data in Fig. 28 has a significantly larger average value of optical thickness than the data in Fig. 17. Most particularly, another maximum frequency of optical thickness is shown at 12 μm in Fig. 43a. The average larger optical thickness in Fig. 43 spreads the distribution of the differences in optical thicknesses in Fig. 43b and takes more optical thickness reductions in the screen of Fig. 28. Figure 44a shows a larger variance in the retrieved cloud-top temperatures than Fig. 41a. The patterns of Figs. 44b and 44c are the same as Figs. 41b and 41c, which indicate little effect of surface roughness on the retrieval of cloud-top temperatures.

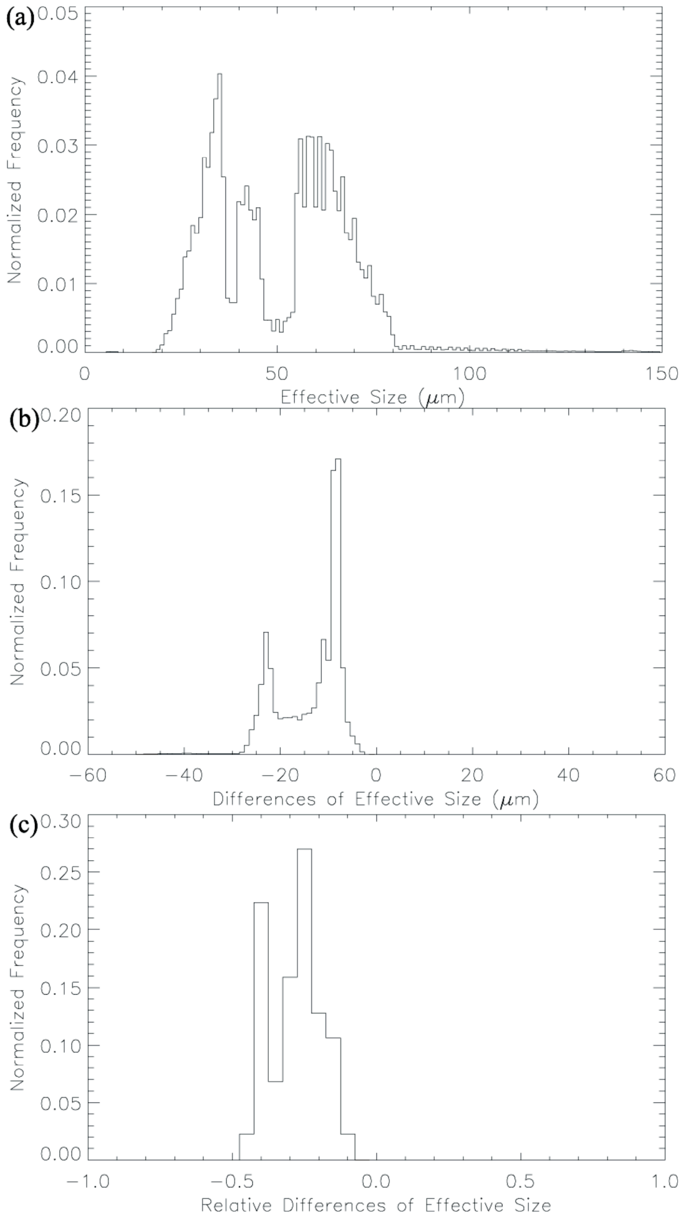

Fig. 42. Histograms of (a) ice cloud effective particle sizes, (b) differences between ice cloud effective particle sizes between using surface smooth and deeply rough particle models, (c) relative differences between ice cloud effective particle sizes using surface smooth and deeply rough particle models for the MODIS granule shown in Fig. 28.

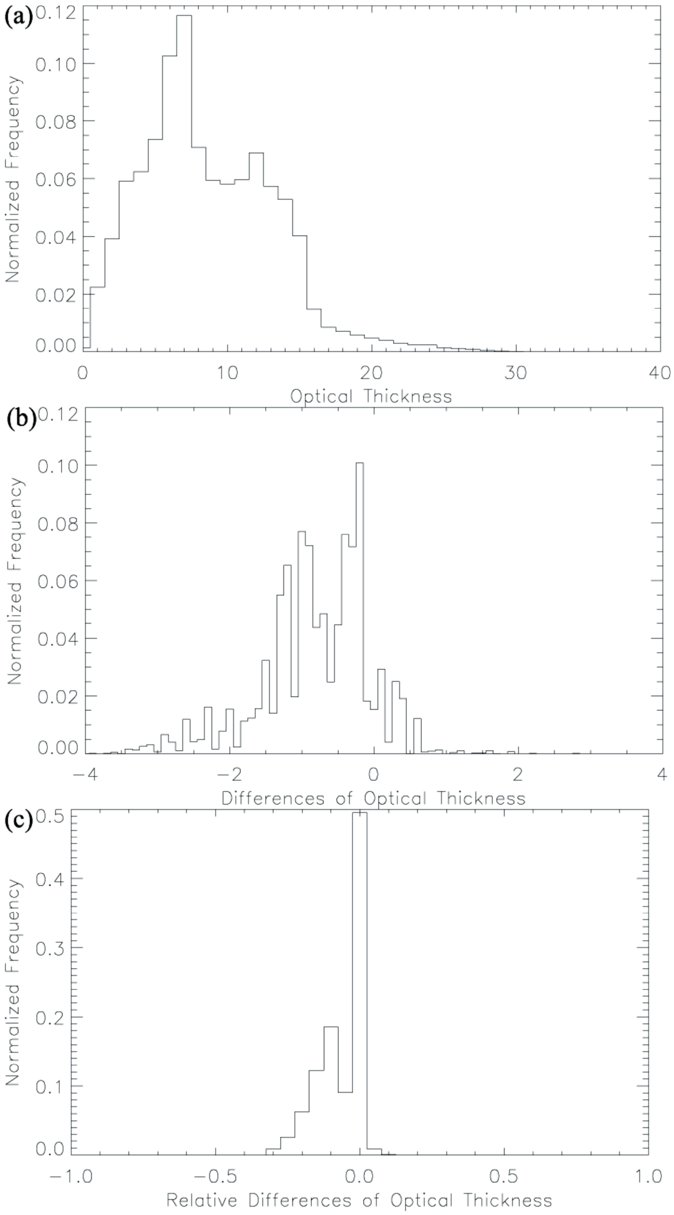

Fig. 43. Histograms of (a) ice cloud optical thicknesses, (b) differences between ice cloud optical thicknesses using surface smooth and deeply rough particle models, (c) relative differences between ice cloud optical thicknesses using surface smooth and deeply rough particle models for the MODIS granule shown in Fig. 28.

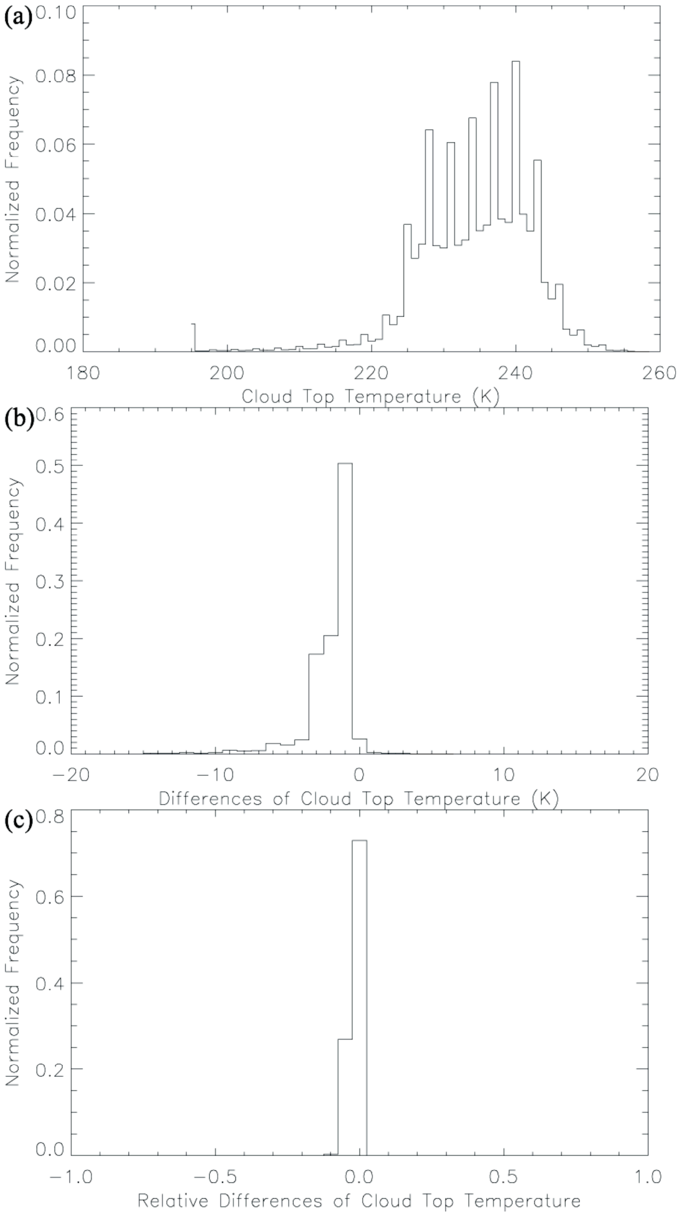

Fig. 44. Histograms of (a) cloud-top temperatures, (b) differences between cloud-top temperatures using surface smooth and deeply rough particle models, (c) relative differences between cloud-top temperatures using surface smooth and deeply rough particle models for the MODIS granule shown in Fig. 28.

5. CONCLUSIONS AND DISCUSSION

Global retrievals of ice cloud microphysical and optical properties require a knowledge of ice crystal single-scattering properties which can be intensively affected by particle habits, shapes and surface roughness conditions. To address this need, a considerable research has been done to develop single-scattering models with a variety of ice crystal habit and size distributions. However, the surface roughness has been routinely ignored in most of those efforts. The thrust of this study is to improve the understanding of the effect of ice crystal surface roughness on single-scattering properties and retrieval of cloud microphysical and optical properties from MODIS data.

In this study, a composite method has been used to compute the single-scattering properties of ice cloud with the assumption that ice clouds consist of hexagonal columns with a variation in aspect ratios and particle surface roughness conditions. The resulting ice cloud bulk-scattering properties are then given by employing 11 particle size distributions based on in situ measurements. These ice cloud microphysical and optical properties have demonstrated a parameterization of cloud bidirectional reflectance and emittance in terms of cloud particle size, optical thickness, cloud-top temperature, surface temperature, ice crystal surface roughness and solar and satellite viewing angles. This parameterization was later applied to a 3-channel retrieval algorithm for MODIS data at 0.65, 3.75, and 10.8 μm. Cloud microphysical and optical properties were derived iteratively for each pixel that contained ice clouds. Two granules of MODIS data indicated that the retrieved effective particle sizes are significantly reduced from 20% to 40% by using surface rough particles. However, increasing the degree of surface roughness has little effect on the reduction of effective particle size. In most of the pixels retrieved, the cloud optical thicknesses were also reduced by using surface rough particles. The reductions were increased, in these pixels by increasing the degree of surface roughness. However, converted results of cloud optical thickness were shown in some specific areas with relatively large cloud optical thickness and high cloud-top temperatures. It was also found that surface roughness has a very minor effect on the retrieval of cloud-top temperatures because of the relatively slight roughness compared to the long wavelength.

This study, including the development of 3-channel retrieval algorithm and the research of the effect of surface roughness on MODIS retrieval, is still under construction. More future research is needed to improve this study. First of all, the center wavelengths were used in each band of the single-scattering computations in this study. This was good approximation for the visible channel, λ=0.65 μm, because the real part of the refractive index varies slightly and the imaginary part is close to 0 in that channel. However, the response functions of the bands are influenced by the solar constants decreasing in infrared channels. Thus, it was necessary to employ a weighting function to the single-scattering properties in the infrared bands instead of using a single wavelength. Another issue that may create errors in the retrieval is the determination of atmospheric profiles. For simplification and saving computing time, a standard atmospheric profile was used to compute the optical thickness for each layer in the infrared channels. To remove the error caused by using the same atmospheric profile for each pixel of a MODIS granule, the Atmospheric Infrared Sounder (AIRS) data of temperature and water vapor profiles could be used in the simulation of the clear-sky brightness temperatures.

Validation efforts of our MODIS retrievals are essential to understanding the accuracy of this study. But MODIS Level 2 data cannot be used to verify these results because ice cloud particle habits and size distributions differ from those of the MODIS collection 4 or 5 cloud models. To validate our ice cloud retrieval algorithm, further study is required regarding ice crystal surface roughness and finally employing it to a parameterization of ice cloud single-scattering properties for a variety of wavelength, particle habits and size and surface roughness. This parameterization may include the single-scattering properties of aggregate, bullet-rosette, droxtal, hexagonal column, hollow column and plate, which are implemented for MODIS collection 5 ice cloud models.

Finally, in the future, other MODIS channels could be used in our 3-channel retrieval algorithm. For example, in this study, retrievals were limited to the ocean surfaces to use constant surface emissivities. To avoid this limitation and retrieve ice cloud optical properties from MODIS granules over land, spectral reflectances in a water vapor band of λ=1.38 μm could be used to retrieve ice cloud effective particle size and optical thickness.

REFERENCES

Ardanuy P. A., D. Han, and V. V. Salomonson, 1991: The Moderate Resolution Imaging Spectrometer (MODIS) science and data system requirements, *IEEE Trans. Geosci. Remote Sensing*, **29**, 75-88.

Chandrasekhar S, 1960: *Radiative Transfer*. Dover, New York.

de Hann J. F., P. B. Bosma, J. W. Hovenier, 1987: The adding method for multiple scattering calculations of polarized light. *Astron Astrophys*, **183**, 371-391.

Fu Q., W. B. Sun, and P. Yang, 1999: Modeling of scattering and absorption by nonspherical cirrus ice particles at thermal infrared wavelengths. *J. Atmos. Res.*, **56**, 2937-2947.

Fu Q., P. Yang, and W. B. Sun, 1998: An accurate parameterization of the infrared radiative properties of cirrus clouds for climate models. *J. Clim.*, **25**, 2223-2237.

Garg R, R. K. Prud'homme, I. A. Aksay. 1998: Optical transmission in highly concentrated dispersions. *J. Opt. Soc. Am. A.*, **15**, 932-935.

Guimaraes L. G., and H. M. Nussenzveig, 1992: Theory of Mie resonancees and the ripple fluctuations. *Opt. Commun.*, **89**, 363-369.

Hapke B. 1993: *Theory of Reflectance and Emittance Spectroscopy*. Cambridge University, New York.

Heymsfield A. J and Platt C. M. R., 1984: A parameterization of the particle size spectrum of ice clouds in terms of the amient temperature and the ice water content. *J. Atmos. Sci.*, **41**, 846-855.

Heymsfield A. J., 1977: Precipitation development in stratiform ice clouds: A microphysical and dynamical study. *J. Atmos. Sci.*, **34**, 367-381.

Huang H. L., P. Yang, H. Wei, B. A. Baum, Y. Hu, P. Antonelli, and S. A. Ackerman, 2004: Inference of ice cloud properties from high spectral resolution infrared observations, *IEEE Trans. Geosci. Remote Sens*., **42**, 842-853.

Hu Y. X., B. Wielicki, B. Lin, G. Gibson, S. C. Tsay, K. Stamnes, T. Wong, 2000: δ-Fit: A fast and accurate treatment of particle scattering phase functions with weighted singular-value decomposition least-squares fitting. *J. Quant. Spectrosc. Radiat. Transfer*, **65**, 681-690.

Kattawar G. W., G. N. Plass, 1973: Interior Radiances in optically deep absorbing media—I exact solutions for one-dimensional model. *J. Quant. Spectrosc. Radiat. Transfer*, **13**, 1065-1080.

Kiehl J. T and K. E. Trenberth, 1997: Earth's annual global mean energy budget. *Bull. Am. Meteorol. Soc.*, **78**, 197-208.

King M. D., Y. J. Kaufman, W. P. Menzel, and D. Tanre, 1992: Remote sensing of cloud, aerosol, and water vapor properties from the Moderate Resolution Imaging Spectrometer (MODIS), *IEEE Trans. Geosci. Remote Sensing*, **30**, 2-27.

King M. D., W. P. Menzel, Y. J. Kaufman, D. Tanre, B. C. Gao, S. Platnick, S. A. Ackerman, L. A. Remer, R. Pincus, and P. A. Hubanks, 2003: Cloud and aerosol properties, precipitable water, and profiles of temperature and water vapor from MODIS, *IEEE Trans. Geosci. Remote Sensing*, **41**, 442-458.

King M. D., S. Platnick, P. Yang, G. T. Arnold, M. A. Gray, J. C. Riedi, S. A. Ackerman, and K. N. Liou, 2004: Remote sensing of liquid water and ice cloud optical thickness and effective radius in the Arctic: application of airborne multispectral MAS data. *J. Atmos. Oce. Tec.*, **21**, 857-875.

Korolev A. and G. Isaac, 2003: Roundness and aspect ratio of particles in ice clouds. *J. Atmos. Sci.*, **60**, 1795-1808.

Kratz D. P., 1995: The correlated-k distribution technique as applied to the AVHRR channels, *J. Quant. Spectrosc. Radiat. Transfer.*, **53**, 501-517.

Li S., and X. Zhou, 2004: Modeling and measuring the spectral bidirectional reflectance factor of snow-covered sea ice: an intercomparison study. *Hydrol Processes*, **18**, 3559-3581.

Liou K. N., 1986: Influence of cirrus clouds on weather and climate processes: A global perspective. *Mon. Wea. Rev.*, **114**, 1167-1199.

Liou K. N., 1972: Light scattering by ice clouds in the visible and infrared: a theoretical study. *J. Atmos, Sci.,* **29**, 524-536.

Liou K. N., Y. Takano, and P. Yang, 1999: *Light scattering and radiative transfer in ice crystal clouds: applications to climate research, in Light Scattering by Nonspherical Particles*. Academic. 417 pp.

Meyer K., P. Yang, and B. C. Gao, 2004: Optical thickness of tropical cirrus clouds derived from the MODIS 0.66 and 1.375 μm channels, *IEEE Trans. Geosci. Remote Sens.*, **42**, 833-841.

Minnis P., D. P. Garber, D. F. Young, R. F. Arduini, and Y. Takano, 1998: Parameterizations of reflectance and effective emittance for satellite remote sensing of cloud properties. *J. Atmos. Sci.*, **55**, 3313-3339.

Minnis, P., D. P. Kratz, J. A. Coakley, M. D. King, D. Garber, P. Heck, S. Mayor, D. F. Young, and R. Arduini, 1995: Cloud Optical Property Retrieval (Subsystem 4.3). Clouds and the Earth's Radiant Energy System (CERES) Algorithm Theoretical Basis Document, Volume III: Cloud Analyses and Radiance Inversions (Subsystem 4) *NASA RP 1376*, **3**, 135-176.

Minnis P., P. W. Heck, and D. F. Young, 1993: Inference of cirrus cloud properties from satellite-bserved visible and infrared radiances. Part II: Verification of theoretical radiative properties. *J. Atmos. Sci*., **50**, 1305-1322.

Mishchenko M. I., 2002: Vector radiative transfer equation for arbitrarily shaped and arbitrarily oriented particles: a microphysical derivation from statistical electromagnetics. *Appl. Opt*., **41**, 7114-7134.

Mishchenko M. I., 1994: Asymmetry parameters of the phase function for densely packed scattering grains. *J. Quant. Spectrosc. Radiat. Transfer*, **52**, 95-110.

Mishchenko M. I., L. D. Travis, A. A. Lacis, 2005: *Multiple Scattering of Light by Particles: Radiative Transfer and Coherent Backscattering*. Cambridge University Press.

Mishchenko M. I., J. M. Dlugach, E. G. Yanovitskij, N. T. Zakharova, 1999: Bidirectional reflectance of flat, optically thick particulate layers: an efficient radiative transfer solution and applications to snow and soil surfaces. *J. Quant. Spectrosc. Radiat. Transfer*, **63**, 409-432.

Nakajima T., and M. D. King, 1990: Determination of the optical thickness and effective particle radius of clouds from reflected solar radiation measurements. Part 1: theory, *J. Atmos. Sci*., **47**, 1878-1893.

Ou S. C., K. N. Liou, W. M. Gooch, and Y. Takano, 1993: Remote sensing of cirrus cloud parameters using Advanced Very High Resolution Radiometer 3.7 and 10.9 μm channels. Appl. Opt., 32, 2171-2180.

Perrin J. M. and J. P. Sivan, 1991: Scattering and polarization of light by rough and porous interstellar grains. *Astron. Astrophys.*, **247**, 497-504.

Poelot M. R., and B. Henderson, 1994: *Univeristy of North Dakota citation FIRE Cirrus II mission summary and data report*. 207 pp.

Rolland P., K. N. Liou, M. D. King, S. C. Tsay, and G. M. McFarquhar, 2000: Remote sensing of optical and microphysical properties of cirrus clouds using Moderate-Resolution Imaging Spectroradiometer channels: Methodology and sensitivity to physical assumptions. *J. Geo. Res.*, **105**, 11,721-11,738.

Stamnes K, S. S. C. Tsay, W. Wiscombe, K. Jayaweera, 1988: Numerically stable algorithm for discrete-ordinate-method radiative transfer in multiple scattering and emitting layered media. *Appl. Opt.*, **27**, 2502-2509.

Takano Y and K. N. Liou, 1989: Solar radiative transfer in cirrus clouds. Part I: single-scattering and optical properties of hexagonal ice crystals. *J. Atmos. Sci.*, **46**, 3-19.

van de Hulst H. C., 1963: *A New Look at Multiple Scattering. Goddard Institute for Space Studies*. New York.

Wei H., P. Yang, J. Li, B. A. Baum, H. L. Huang, S. Platnick, Y. Hu, and L. Strow, 2004: Retrieval of semitransparent ice cloud optical thickness from Atmospheric Infrared Sounder (AIRS) measurement. *IEEE Trans. Geosci. Remote Sens.*, **42**, 2254-2267.

Wiscombe W. J., 1979: Improved Mie scattering algorithms. *Appl. Opt.*, **19**, 1505-1509.

Wiscombe W. J., 1977: The delta-M method: rapid yet accurate radiative flux calculations for strongly asymmetric phase functions. *J Atmos Sci.*, **34**, 1408-1422.

Wylie D. P., W. P. Menzel, H. M. Woolf, and K. I. Strabala, 1994: Four years of global cirrus cloud statistics using HIRS. *J. Climate*, **7**, 1972-1986.

Xie Y., P. Yang, B. C. Gao, G. W. Kattawar, and M. I. Mishchenko, 2006: Effect of ice crystal shape and effective size on snow bidirectional reflectance. *J. Quant. Spectrosc. Radiat. Transfer*, **100**, 457-469.

Yang P. and K. N. Liou, 1996: Finite-difference time domain method for light scattering by small ice crystals in three-dimensional space. *J. Opt. Soc. Amer.*, **A13**, 2072-2085.

Yang P. and K. N. Liou, 1996: Geometric-optics-integral-equation method for light scattering by nonspherical ice crystals. *Appl. Opt.*, **35**, 6568-6584.

Yang. P., H. L. Wei, H. Huang, B. A. Baum, Y. X. Hu, G. W. Kattawar, M. I. Mishchenko, and Q. Fu, 2005: Scattering and absorption property database for nonspherical ice particles in the near-through far-infrared spectral region. *Appl. Opt.*, **44**, 5512-5523.

Yanovitskij E. G., 1997: *Light scattering in inhomogeneous atmospheres*. Berlin: Springer.

Zhang H., and K. J. Voss, 2005: Comparisons of bidirectional reflectance distribution function measurements on prepared particulate surfaces and radiative-transfer models. *Appl. Opt.*, **44**, 597-610.

VITA

Biography

Yu Xie received his Bachelor of Science degree in physics at Peking University in Beijing in July 2003. He continued his study in Department of Atmospheric Sciences at Texas A&M University beginning in September 2004, and received his Master of Science degree in May 2007.

Mr. Xie will continue his studies in the Department of Atmospheric Sciences at Texas A&M University beginning in May 2007. He may be reached at the Department of Atmospheric Sciences, Texas A&M University, 3150 TAMU, College Station, TX77843. His email address is xieyu@ariel.met.tamu.edu.

Publications

Xie Y., P. Yang, B. C. Gao, G. W. Kattawar, and M. I. Mishchenko, 2006: Effect of ice crystal shape and effective size on snow bidirectional reflectance. *J. Quant. Spectrosc. Radiat. Transfer*, **100**, 457-469.

Lawless R., Y. Xie, P. Yang, G. W. Kattawar, and I. Laszlo, 2006: Polarization and effective Muller matrix for multiple scattering of light by nonspherical ice crystals. *Optics Express*, **14**, 6381-6393.